CSIRO
AUSTRALIA

Radiation fluxes and cloud amounts predicted by the CSIRO nine level GCM and observed by ERBE and ISCCP

D.M. O'Brien

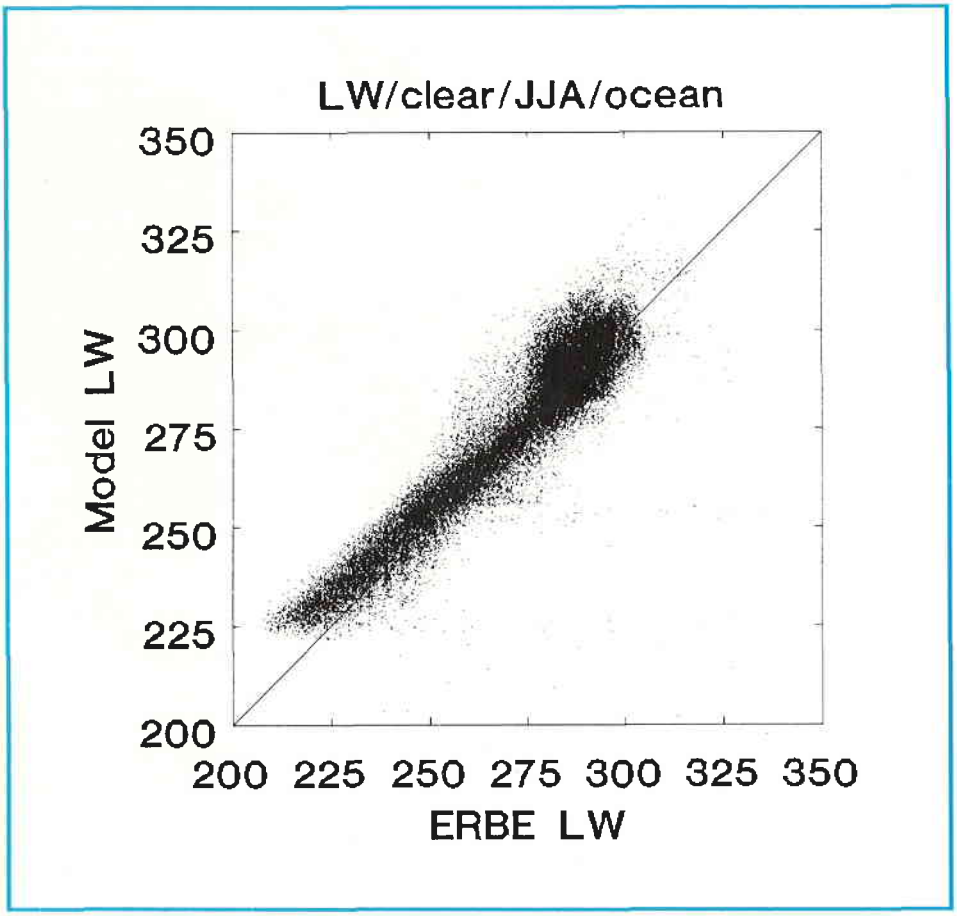

CSIRO DIVISION OF ATMOSPHERIC RESEARCH TECHNICAL PAPER
NO. 30

Radiation fluxes and cloud amounts predicted by the CSIRO nine level GCM and observed by ERBE and ISCCP

D.M. O'Brien

DIVISION OF ATMOSPHERIC RESEARCH TECHNICAL PAPER
NO. 30

National Library of Australia Cataloguing-in-Publication Entry

O'Brien, D.M.
Radiation fluxes and cloud amounts predicted by the CSIRO nine level GCM and observed by ERBE and ISCCP.

Bibliography.
ISBN 0 643 05253 4.

1. Atmospheric radiation—Mathematical models. 2. Clouds—Mathematical models. I. CSIRO. Division of Atmospheric Research. II. Title. (Series: CSIRO Division of Atmospheric Research Technical Paper; no. 30).

551.52730151

CSIRO Division of Atmospheric Research Technical Papers may be issued out of sequence.

Front cover: Comparison of clear sky long wave flux density at the top of the atmosphere predicted by the GCM and observed by ERBE over the sea for the June, July and August season.

Printed on recycled, environmentally friendly paper

Radiation fluxes and cloud amounts predicted by the CSIRO nine level GCM and observed by ERBE and ISCCP

D.M. O'Brien
CSIRO Division of Atmospheric Research
Private bag 1, Mordialloc, Victoria 3195
Australia

Abstract
The International Satellite Cloud Climatology Project (ISCCP) and the Earth Radiation Budget Experiment (ERBE) have provided global data on cloud and the radiation fluxes at the top of the atmosphere. These data are used to assess the performance of the cloud and radiation parameterizations of the CSIRO nine level GCM. The configuration of the GCM is that used in the Atmospheric Model Intercomparison Project (AMIP) for which sea surface temperatures were prescribed. The essential findings of the report are as follows.
(1) Over the ocean, where the surface temperature, emissivity and albedo are known reliably, the parameterizations of clear sky long wave (LW) and short wave (SW) flux densities appear to be accurate to $\pm 5\,\mathrm{Wm}^{-2}$ for monthly and regionally ($2.5° \times 2.5°$) averages.
(2) The clear sky LW flux density over land and desert is too high in June, July and August, particularly in the northern hemisphere. The bias can be attributed to errors in the surface temperature and emissivity.
(3) The AMIP configuration of the GCM used land albedos published by Posey and Clapp. It is well known that these albedos are too low over land and desert, a result confirmed by the present comparison.
(4) The GCM parameterizes the albedo of snow covered land in terms of the snow depth. The albedo attains a maximum when the snow depth reaches a critical depth d_0. There is evidence to suggest that d_0 is too small in the AMIP configuration of the GCM.
(5) Cloud fraction is predicted poorly by the GCM, particularly in the tropics.
(6) Errors in both the LW and SW flux density are strongly correlated with errors in cloud amount. The scatter of the GCM predictions is largest over the tropical oceans. The scatter would be reduced significantly if the cloud amount were predicted more accurately.

1 Introduction

As a result of international satellite programs, such as the Earth Radiation Budget Experiment (ERBE) and the International Satellite Cloud Climatology Project (ISCCP), data bases of radiation fluxes at the top of the atmosphere (TOA), cloud properties and profiles of temperature and water vapour are now readily available. These data enable assessment of the performance of atmospheric general circulation models (GCMs) in ways previously impossible (Briegleb et al. 1986, Harshvardan et al. 1989, Wetherald et al. 1991).

Considerable care must be exercised in comparing GCM predictions with satellite data. Firstly, it is essential that the GCM simulate the spatial and temporal sampling of the satellite instruments in order to ensure that like quantities are being compared. More fundamental is the question of climate predictability. GCMs rapidly lose all memory of the initial state and degenerate into a state of deterministic chaos, so only ensemble and time averages retain information about climate. On the other hand, satellite data are observations of the state of planet earth at a particular time. Therefore, one should not expect the GCM to reproduce the satellite data, except in a rather imprecisely defined climate average.

However, there is one circumstance in which a GCM might be expected to predict the observed state of the earth, namely, when the GCM is forced by monthly observed sea surface temperatures rather than by climatological average temperatures. Such a climate simulation was performed with the CSIRO nine level GCM (CSIRO-9) as part of the Atmospheric Model Intercomparison Project (AMIP), described by Gates (1992). The climate simulation was from January 1979 to December 1988 with sea surface temperatures and sea ice extent prescribed over this period from both surface and satellite observations. The run overlapped the ERBE observations (February 85–July 88) and ISCCP (July 83–present), so it was decided to compare GCM and satellite data over the ERBE period with the express purpose of assessing the performance of the radiation and cloud parameterizations of the GCM. It was hoped that areas where the model is weakest, and hence where research effort would be best directed, might be diagnosed from careful scrutiny of the comparisons. A secondary aim was to document the performance of the GCM in the form used for AMIP as a benchmark against which future versions of the GCM could be compared.

It must be stressed that an early version of CSIRO-9 was used for AMIP, and that many of the deficiencies noted in this report have been corrected by subsequent improvements to the GCM. In particular, the current code includes an improved cloud scheme, a new surface scheme, including albedos from the simple biosphere model (SiB) of Sellers et al. (1986), a modified snow scheme and a new albedo-snow depth relation. A comparison of the predictions of the latest version of the GCM with observations from ERBE and ISCCP should show substantially better agreement.

The sensitivity of climate models to various forcing mechanisms has been examined by Cess et al. (1990), who compared the performance of 19 GCMs and found that a "first order priority for further model improvement is the treatment of clouds within GCMs". Therefore, it is not surprising that the principal conclusions from this study are that: (1) the parameterization of radiation used by the GCM is reliable in clear sky over targets with known albedo, emissivity and surface temperature; (2) the largest uncertainties are associated with the prediction of cloud.

The comparisons are presented in the form of scatter plots. The GCM, ERBE and ISCCP data have been interpolated to a common 2.5° × 2.5° latitude and longitude grid. The data are monthly averages of daily averaged values. Each point on a scatter plot represents data from one month for one grid square. Only points in the latitude band from 60° N to 60° S have been used, primarily because at higher latitudes the detection of cloud cover over snow is difficult from space.

The scatter plots typically have GCM predictions along one axis and satellite observations along the other. Perfect agreement would be indicated by a diagonal line. Two quantities are important in each plot, the bias, or deviation of the line of best fit from the diagonal line, and the scatter of points about the line of best fit. The bias must be small, not only globally but also regionally if the GCM is to predict regional climate change. The scatter arises from errors in the GCM's parameterizations and also from the chaotic, unpredictable nature of climate.

Three measures of scatter are used in this report. The first, denoted E, is the root-mean-square (rms) deviation of the GCM predictions $(y_1, y_2, \ldots)$ from the satellite observations $(x_1, x_2, \ldots)$ taken over all points in the scatter plot:

$$E = \left(\frac{1}{n} \sum_{i=1}^{n} (y_i - x_i)^2 \right)^{1/2} . \tag{1}$$

The second, E_+, is the rms deviation of the n_+ points where the GCM prediction exceeds the satellite observations,

$$E_+ = \left(\frac{1}{n_+} \sum_{y_i > x_i} (y_i - x_i)^2 \right)^{1/2} . \tag{2}$$

Lastly, E_- is the rms variance of the complementary set,

$$E_- = \left(\frac{1}{n_-} \sum_{y_i < x_i} (y_i - x_i)^2 \right)^{1/2} . \tag{3}$$

A good correlation between GCM and satellite data generally will have $n_+ \approx n_-$ and $E \approx E_+ \approx E_-$, consistent with the identity

$$nE^2 = n_+ E_+^2 + n_- E_-^2 . \tag{4}$$

The discrepancy between E_+ and E_- will be large if the diagonal line of perfect correlation is a poor fit to the points of the scatter plot. Consequently,

$$B = E_+ - E_- \tag{5}$$

will be used as a measure of the bias in the GCM predictions.

In this report the scatter is exploited to diagnose weaknesses in the radiation and cloud parameterizations. To do so, differences between GCM and satellite data in one variable are correlated with corresponding differences in other variables. Several strong correlations emerge, in particular between errors in cloud amount and errors in both short wave (SW) and long wave (LW) flux densities. Subsequent regional analysis identifies where the physics of the GCM is in error.

Details of the GCM and its configuration for the AMIP runs are given by McGregor et al. (1992). The LW parameterization is the 'simplified exchange method' of Schwartzkopf and Fels (1991). The SW code is derived from Lacis and Hansen (1974). The ERBE instruments, satellites and data processing system are described by Kopia (1986), Barkstrom (1984), and Barkstrom et al. (1989). The ERBE data set contains monthly means of daily averaged values of planetary albedo and short wave, long wave and net flux density for both clear and cloudy sky. Cloudy sky refers to the observed sky, consisting of patches of clear sky and patches of cloud. The accuracy of the radiation fluxes is estimated to be $\pm 5\,\mathrm{Wm}^{-2}$ for monthly and regional averages over $2.5° \times 2.5°$ latitude and longitude grid squares (Barkstrom et al., 1989). Each grid square is classified by ERBE as either ocean, land, snow, desert or coast. The ISCCP data are taken from the C2 data set described by Rossow (1989) and Rossow and Schiffer (1991). The variable of most interest in this study is the mean frequency of cloudy pixels within each grid square.

The ERBE and ISCCP data sets are the best available for TOA radiation fluxes and cloud properties. However, it is recognized that both ERBE and ISCCP are subject to errors and misinterpretation, even though in this report departures of the GCM predictions from ERBE or ISCCP are occasionally referred to as errors. The major limitations of the ERBE data are as follows.

1. The data are not direct observations of flux density at the top of the atmosphere (TOA), but rather are obtained by inverting observations at the satellite altitude to TOA, a process which requires independent data for the angular distribution of radiance leaving the atmosphere.

2. The ERBE sampling strategy is not easily simulated by GCMs, a point carefully examined by Cess et al. (1992), who found for the ECMWF GCM that errors of approximately $\pm 3\,\mathrm{Wm}^{-2}$ can be introduced by changing the sampling strategy. However, the differences noted in this report between GCM predictions and satellite observations are much larger, so the precise mechanism by which the GCM simulates the ERBE sampling may be neglected temporarily.

3. The clear sky observations of ERBE are determined from ERBE scanner pixels diagnosed as clear. Because the scanner footprint is approximately 35 km in diameter, the likelihood of a small amount of cloud contamination is high. Furthermore, the temporal sampling is determined not only by the satellite orbit and the scan geometry, but also by the chance occurrence of clear sky. Thus, there are fewer clear than cloudy sky observations in each grid square, and the temporal sampling may be biased towards times of the day when cloudiness is at a minimum. Raval and Ramanathan (1989) applied a rigorous test for clear pixels in ERBE data and found that the cloud errors were no more than $\pm 4\,\mathrm{Wm}^{-2}$ for the LW flux density.

4. The ERBE experiment involved three satellites, two in polar orbits with fixed local overpass times, and a third (ERBS) in a low inclination orbit to ensure more uniform temporal sampling. The orbit of ERBS guaranteed that every grid square would be sampled at every hour of the day in the course of a month, the repetition period of the satellite. Despite the care taken with subsequent

processing, some doubt must remain as to whether the diurnal cycle has been correctly sampled by ERBE.

ISCCP cloud amounts are thought to be reliable, but cloud optical properties are suspect. In particular, Klein and Hartmann (1993) reported that an apparent drift in optical thickness is more likely to have been a result of sensor calibration than a physical effect.

The longwave and shortwave flux densities at the top of the atmosphere will be denoted by F_{LW} and F_{SW}. Units are Wm^{-2}. Cloud amount will be denoted by C. Predictions of the parameters by the GCM will be indicated by a superscript m (for model), while satellite data will have a superscript s (for satellite). For example, F^m_{LW} and F^s_{LW} will represent the GCM and ERBE values of F_{LW}, respectively. Similarly, C^m and C^s are the GCM and ISCCP cloud amounts, respectively.

The scatter plots comparing GCM and satellite data are presented in three groups. The first group contains direct comparisons of GCM predictions with either ERBE or ISCCP observations in both clear and cloudy skies. Each page shows one physical variable for either the June, July, August (JJA) season or the December, January, February (DJF) season. There are four plots on each page, corresponding to the ERBE surface classifications of ocean, land, snow and desert. The facing page contains analogous results for the other season. The second group contains scatter plots of the differences between GCM and ERBE flux densities against differences between GCM and ISCCP cloud amounts. The format for each page is the same as for group 1. The third group contains both direct comparisons and correlations of differences, but the plots have been analysed into southern, tropical and northern zones. The format of these pages will be explained later in the text.

No attempt will be made to comment upon every plot, particularly as many are self explanatory. Rather, attention will be focused upon those plots which highlight the performance of the radiation parameterizations of the GCM.

2 Clear sky flux density

2.1 LW flux density

Figure 1 compares the predictions of the GCM with ERBE observations of the LW flux density at the top of the atmosphere in clear sky for the months of June, July and August (JJA) in the years 1985–1988. The surface categories of ocean, land, snow and desert are shown separately.

Over the ocean the rms scatter is $E = 7.3\,\mathrm{Wm}^{-2}$ and the bias is small, with $E_+ = 7.8\,\mathrm{Wm}^{-2}$ and $E_- = 6.0\,\mathrm{Wm}^{-2}$. Although the difference between E_+ and E_- is numerically small, it is important to note that F^m_{LW} shows a consistent high bias over colder targets. Good agreement is to be expected because the GCM used prescribed daily sea surface temperatures, obtained by interpolation from monthly averaged satellite observations. In clear sky, the LW flux density at the top of the atmosphere consists of about 70% from the surface and 30% from the atmosphere. The latter component is determined primarily by the temperature and water vapour profiles, both of which can be modelled in the first approximation by the climatological averages. Thus, good agreement is contingent upon good surface temperatures, in this case guaranteed. The situation shown in figure 2 for December, January and February (DJF) is similar.

In JJA over land and desert, the rms scatter in the LW flux density is not only larger ($E = 14\,\mathrm{Wm}^{-2}$), but also the GCM flux density is biased too high with $B \approx 7\,\mathrm{Wm}^{-2}$. It is unlikely that the errors are introduced by the clear sky LW radiation parameterization, because the parameterization is the same over both ocean and land, and the errors are small in the former case where the temperature and emissivity are known. Therefore, the bias must arise from incorrect surface temperatures, errors in assigned emissivities, or errors in the water vapour and temperature profiles. Because profile errors have only a secondary effect, the first two candidates are more likely. The emissivity of the surface is assumed to be unity in the GCM, leading to large errors over deserts and smaller errors over vegetated surfaces and oceans. Watterson et al. (1993) have already noted a warm bias in surface temperature over the northern hemisphere land masses.

The LW data used in these comparisons are derived primarily from the ERBE scanner instruments. Because the scanner pixels are large ($\approx$35 km), the possibility of undetected cloud within ERBE pixels must be considered, particularly as the differences over land just attributed to a warm bias in the GCM might also be explained by undetected cloud in the observations. Indeed, over the ocean, where cloud is more easily detected against the dark, warm background, the LW flux density comparison shows no significant bias. However, over land and snow, where cloud is difficult to detect, a small amount of undetected cloud would bias F^s_{LW} too low, consistent with the JJA situation shown in figure 1.

The counter to this argument is provided by the DJF observations in figure 2. In the northern winter, with increased snow cover and presumably greater difficulty in detecting cloud, the bias in F^m_{LW} over land and desert is reduced. Because the same processing algorithm is used for both seasons, it is unlikely that undetected cloud could cause a bias in the data in one season but not the other. Thus, the inference stands that the land and desert emissivities and temperatures are too high in the GCM in JJA.

Over snow in JJA, F^m_{LW} is far too high. Because the value is comparable to the flux density over land, it is probable that the GCM has diagnosed the surface as land, whereas ERBE has classified the surface as snow. An alternative explanation might be that the temperature assigned to the snow by the GCM is too high. The high bias of the GCM over snow persists in DJF.

2.2 SW flux density

Figures 3 and 4 compare GCM predictions and ERBE observations of the clear sky SW flux density at the top of the atmosphere for the JJA and DJF seasons.

Over the ocean, a target whose albedo is known accurately, the agreement is generally good, except for a cluster of points where F^m_{SW} is impossibly high for the ocean and unlikely even for cloud. The most probable explanation is that the GCM has diagnosed sea ice and assigned a high albedo, while ERBE has observed clear ocean. The rms scatter of the remaining points is $E \approx 6\,\mathrm{Wm}^{-2}$ and the bias is smaller with $B = 4.8\,\mathrm{Wm}^{-2}$ in JJA and $B = 1.3\,\mathrm{Wm}^{-2}$ in DJF.

Over land and desert in both JJA and DJF, F^m_{SW} shows wide scatter and a significant low bias. Again there is a cluster of points where the GCM has F_{SW} too high, presumably because the GCM diagnosed snow. The only significant difference in the

SW parameterization between ocean and land is the higher albedo of land, because the parameterization of molecular scattering and absorption by water vapour and O_3 is the same for both. Therefore, the land and desert albedos, taken from Posey and Clapp (1964), are too low. This deficiency was noted earlier by Garratt et al. (1993). The discrepancy in the clear sky F_{SW} is even larger over desert, indicating correspondingly larger errors in the albedo.

The GCM assigns an albedo to snow covered land which depends upon snow depth d according to

$$a = \begin{cases} a_{land} + (a_{snow} - a_{land})\sqrt{d/d_0} & \text{if } d < d_0. \\ a_{snow} & \text{if } d \geq d_0. \end{cases} \quad (6)$$

The land albedo, a_{land}, is taken from the Posey and Clapp (1964) data set, while a_{snow} is either 0.8 or 0.5, depending on whether the snow is dry or melting. Thus, the albedo of snow in the GCM rises rapidly from a_{land} to a_{snow} once the snow depth has reached d_0. In the AMIP simulations, the critical snow depth, d_0, was assumed to be 100 mm.

In the northern winter, land and desert points are clustered along two lines. The upper line corresponds to land classified as clear by ERBE, but to which the GCM has assigned the higher albedo a_{snow}. The model has either precipitated too much snow, or the snow albedo relation rises too quickly with snow depth. If the latter is the case, then the obvious remedy would be to increase d_0, the critical depth at which the snow covered land reaches the maximum albedo a_{snow}. This question has been addressed in subsequent versions of the GCM.

In the figure showing points classified as snow by ERBE, the points fill a wedge defined by two bounding lines. Points above the diagonal line cluster in bands because at high latitudes the GCM assigns the same albedo to all snow covered boxes in a latitude band, whereas ERBE sees a range of albedos. These points are too high, compared with ERBE, suggesting that the albedo assigned by the GCM is too high. Either the snow albedo is not as high as the model assumes, or the snow is not as deep, or the critical depth d_0 is too small. The remaining points are more evenly scattered between the bounding lines. It is probable that they correspond to land, classified as snow by ERBE, but which in reality is only partially snow covered. The albedo of such land will cover a wide range. The GCM will also predict a range of albedos, determined by the snow depth.

3 Cloud fraction

It is a challenging task for a GCM to predict cloud fraction, even on grid squares as large as $2.5° \times 2.5°$ in latitude and longitude. Nevertheless, if a GCM is to be used in estimating regional impacts arising from increases in greenhouse gases in the atmosphere, then the climatological average of the cloud amount must be approximately correct.

Figures 5 and 6 show the correlation between cloud amount predicted by the GCM and observed by ISCCP. The surface types are those determined by ERBE.

In both JJA and DJF, the GCM predicts too little cloud over the ocean (rms scatter $E = 0.26$ and bias $B = 0.14$). This does not appear to be simply an error in predicting total water vapour, because figures 7 and 8 show reasonable agreement between the integrated water vapour column (in units of $\mathrm{kg\,m^{-2}}$) predicted by the

GCM and retrieved from TOVS. The difference in cloud fraction must be associated with either the temperature profile, the water vapour profile, or the mechanisms for water vapour transport and cloud formation.

Satellite cloud amounts must be used with caution. Firstly, high cloud will mask lower layers from the satellite instruments, so one might expect that total cloud cover measured by satellite would be less than the GCM cloud, predicted on the assumption of random overlap of low, middle and high cloud. That the evidence shows the opposite trend lends support to the conclusion that the GCM cloud is in error. A second issue is the difficulty of detecting cloud over bright, cold surfaces, such as snow, and warm, moist surfaces, such as in the tropics, where high water vapour emission impedes the detection of low cloud at night. Cloud estimation from satellite data is most reliable over the oceans, because the oceans are both dark and warm, enhancing contrast in both the visible and infrared channels.

The ISCCP cloud amounts are derived primarily from geostationary satellite observations, with samples taken at half hourly intervals. Thus, the ISCCP observations span the full diurnal cycle, as do the GCM predictions, so the two can justifiably be compared. Data from polar orbiting satellites are used by ISCCP in polar regions (excluded from this study) and to transfer calibrations between the various geostationary satellites.

Both the bias and the scatter in cloud fraction over land and desert are smaller than over the ocean. Indeed, the only significant bias appears to be over land in JJA ($B = -0.07$), with the GCM cloud amount too low. The rms scatter is typically $E \approx 0.2$.

The JJA snow observations are too few to comment upon, but the DJF plot shows a systematically higher cloud prediction in the GCM compared to ISCCP. Detection of cloud, especially low cloud, over snow covered land from satellite images is very difficult. It is possible that ISCCP has missed cloud, but the poor agreement between GCM and ISCCP over easy targets like the ocean suggests that the GCM also is in error.

Figure 19 compares the cloud amount over the ocean in southern, tropical and northern geographical zones, defined by latitude λ as follows:

$$\begin{array}{ll} \text{S} & -60 < \lambda < -20 \\ \text{T} & -20 < \lambda < +20 \\ \text{N} & +20 < \lambda < +60. \end{array}$$

The bias is at a maximum in the summer hemisphere and the scatter is worst for the tropical region.

4 Cloudy sky flux density

4.1 LW flux density

Given the bias in cloud amount, one might expect a large bias in F_{LW} for cloudy sky. However, figure 9 shows that the scatter over the ocean in JJA is large ($E = 19\,\mathrm{Wm}^{-2}$), but there does not seem to be a significant bias ($B = 4.5\,\mathrm{Wm}^{-2}$). The scatter and the bias are slightly reduced in DJF as shown in figure 10. Cloud physical properties (height, temperature, ...) and optical properties (emissivity, optical thickness, ...)

have been tuned to reduce the bias in F_{LW}. However, the assigned properties must be in error because the cloud amount is in error. The impact upon heating rates could be important for the model and deserves close examination.

The ocean points suggest a cluster, where the GCM/ERBE agreement is good, upon which is superimposed a diffuse pattern of points, where agreement is poor. In particular, the agreement is good at low flux densities, but deteriorates rapidly above a threshold of $\approx 220\,\mathrm{Wm}^{-2}$. Figure 20 analyses the LW flux density in JJA according to the southern, tropical and northern regions defined earlier. The plots in the top row from left to right refer to the zones S,T and N. In region S, the scatter is small and the bias is negligible, yet figure 19 shows that the cloud fraction is too low by $\approx 15\%$. In region T, the points all lie above the diagonal for low F^s_{LW}, but nearly all lie below the diagonal for large F^s_{LW}. The average value of F^m_{LW} is approximately $240\,\mathrm{Wm}^{-2}$when $F^s_{LW} = 200\,\mathrm{Wm}^{-2}$, but is only $290\,\mathrm{Wm}^{-2}$ when $F^s_{LW} = 275\,\mathrm{Wm}^{-2}$. The scatter is uniformly large, with $E \approx 26\,\mathrm{Wm}^{-2}$. Finally, in region N the scatter increases with F^s_{LW}, but the bias is generally small. Figure 21 for DJF has a similar interpretation provided references to N and S in JJA be translated to summer and winter hemisphere.

Over land, snow and desert, the scatter shown for F_{LW} in figures 9 and 10 is large, but only over land in JJA is there a significant bias in the model towards higher values. However, as already noted in the analysis of clear sky F_{LW}, the northern hemisphere land masses appear to be too warm in summer, so the cloudy sky F_{LW} should exhibit a similar bias. The close correlation between GCM and ERBE F_{LW}, despite poor agreement between GCM and ISCCP cloud fraction, indicates that the cloud physical and optical properties are incorrectly assigned over land, snow and desert.

4.2 SW flux density

Many of the deficiencies of the parameterization within the GCM of the cloudy sky LW flux density are reflected in the SW flux density, because the GCM has been tuned to achieve energy balance at the top of the atmosphere. Figures 11 and 12 show the cloudy sky F_{SW} over the four surface types for the JJA and DJF seasons.

Over the ocean the correlation between GCM and ERBE deteriorates suddenly once F_{SW} exceeds a threshold of approximately $50\,\mathrm{Wm}^{-2}$. Breakdowns according to geographical region are presented in figures 22 and 23. In region S in JJA, both the scatter and bias are small, yet the cloud amount is too low, so either the physical or SW optical properties of the cloud are incorrectly assigned. In region T, and to a lesser extent in region N, the points of the scatter plot almost fill a square, indicating negligible correlation between predicted and observed SW flux density. Only at high F_{SW} values in region N does the correlation return.

Over land, snow and desert the biases can be attributed in part to albedo errors, as discussed earlier under the heading of clear sky SW flux density. The rms scatter is unacceptably large, being nearly $30\,\mathrm{Wm}^{-2}$. An attempt to identify the mechanism causing the scatter will be made in the next section.

5 Correlation between errors in flux density and cloud fraction

5.1 LW flux density

In order to probe the causes for differences between F_{LW} predicted by the GCM and observed by ERBE, the LW flux density difference,

$$\Delta F_{LW} = F^m_{LW} - F^s_{LW}, \tag{7}$$

was plotted as a function of the difference in cloud fraction predicted by the GCM and observed by ISCCP,

$$\Delta C = C^m - C^s. \tag{8}$$

Results are shown in figure 15 for the JJA season. For all four surface types there is a strong negative correlation between the LW flux difference and the cloud amount difference. Generally one would expect the flux density and cloud amount to be correlated, with scatter arising from variations in cloud height and temperature. By comparing differences between GCM and satellite observations, the height and temperature dependence will be approximately the same for both, leading to improved correlation.

Over land the points lie approximately on a straight line through the origin, defined by

$$\Delta F_{LW} = \alpha \Delta C. \tag{9}$$

Consequently,

$$F^m_{LW} = F^s_{LW} + \alpha(C^m - C^s), \tag{10}$$

so

$$C^m \approx C^s \quad \text{if} \quad F^m_{LW} \approx F^s_{LW}. \tag{11}$$

The focus of the points has ΔC non-zero, indicating a bias in the cloud fraction, already apparent in the cloud comparison. The peak to peak scatter in the GCM prediction of F_{LW} over land would be reduced to $\pm 20\,\mathrm{Wm}^{-2}$ if the error in the GCM cloud amount could be reduced to $\pm 5\%$. A similar conclusion applies to the desert.

The snow observations in JJA are too few for any pattern to emerge, but the DJF observations show a small bias in ΔF_{LW} and a large positive bias in ΔC of $\approx 30\%$. Because the detection of cloud over snow is difficult, this result should be interpreted with caution.

Cloudy sky LW errors over the ocean are more difficult to analyse. Figure 20 presents a regional analysis of F_{LW} and the correlation between ΔF_{LW} and ΔC for the three geographical regions, S, N and T.

In region S, ΔF_{LW} is small and is tightly correlated with ΔC. The GCM cloud amount is biased too low by approximately 15%, and yet F_{LW} shows little bias, so the GCM must compensate for its underestimate of cloud fraction by increased emission from cloud. This emission is controlled by the emissivity and temperature of the cloud. Although the GCM cloud radiation code allows for specification of cloud emissivity, in the AMIP version it is set to unity for all types of clouds.

In region T the strong negative correlation between ΔF_{LW} and ΔC persists, but there now appear to be two branches, only one of which passes through the origin. The lines of best fit have the forms

$$\Delta F_{LW} = \alpha \Delta C \tag{12}$$

and

$$\Delta F_{LW} = \alpha \Delta C + \beta, \tag{13}$$

where $\beta \approx -10\,\mathrm{Wm}^{-2}$. The peak to peak range of ΔF_{LW} exceeds $100\,\mathrm{Wm}^{-2}$, while ΔC exceeds 1. Despite the serious errors in F_{LW} and C in region T, it remains true that accurate prediction of cloud amount would reduce the peak to peak scatter in ΔF_{LW} to approximately $\pm 25\,\mathrm{Wm}^{-2}$.

In the northern zone, ΔF_{LW} and ΔC are strongly correlated, but the line of best fit does not pass through the origin, indicating that cloud properties have been incorrectly tuned.

The correlations noted for JJA persist in DJF.

5.2 SW flux density

The strong negative correlations between ΔF_{LW} and ΔC are replaced in figures 17 and 18 by strong positive correlations between

$$\Delta F_{SW} = F^m_{SW} - F^s_{SW} \tag{14}$$

and ΔC. Again the most complex situation occurs over the ocean. Figures 22 and 23 show the analyses of the correlations between ΔF_{SW} and ΔC according to regions S, N and T for the JJA season. The peak to peak range of ΔF_{SW} is $\approx \pm 20\,\mathrm{Wm}^{-2}$ in region S, but increases to $\approx \pm 100\,\mathrm{Wm}^{-2}$ in regions T and N. The correlation between ΔF_{SW} and ΔC is strongest in region T, where the line of best fit has the form

$$\Delta F_{SW} = \alpha \Delta C + \beta \tag{15}$$

with $\alpha > 0$ and $\beta > 0$. A similar situation applies in region N. Accurate prediction of cloud amount would reduce the flux error to $\pm 20\,\mathrm{Wm}^{-2}$. An adjustment of the SW optical properties of the cloud would be required.

6 Summary

The version of the CSIRO nine level GCM described by McGregor et al. (1993) was run for a ten year period as part of the Atmospheric Model Intercomparison Project (AMIP). The run overlapped the ERBE and ISCCP observation periods. Because the GCM was strongly forced by prescribed sea surface temperatures, direct comparisons of the SW and LW flux densities at the top of the atmosphere were possible. The principal findings of this report are as follows.

- The ocean is a target with known temperature, emissivity and albedo. Consequently, the accuracy of the GCM parameterizations of F_{LW} and F_{SW} in clear sky can be tested by comparing the GCM predictions with ERBE observations. For both F_{LW} and F_{SW}, the bias appears to be less than $\pm 5\,\mathrm{Wm}^{-2}$.

- Cloud amount predicted by the GCM differs significantly from ISCCP observations. Over the oceans the GCM cloud is low by approximately 15%.

- Differences between the GCM and ERBE flux densities are strongly correlated with differences between GCM and ISCCP cloud amounts. Improving the accuracy of cloud prediction would significantly reduce the errors in the LW and SW flux densities.

- The physical and optical properties of cloud have been tuned to reduce bias in the cloudy sky flux densities. Errors in cloud amount compensate for errors in cloud properties. While this procedure secures overall energy balance, it has the potential to introduce errors into the profile of atmospheric heating.

- Taken together, these observations suggest that the top priority for further work on the cloud and radiation parameterization of the GCM should be the improvement of the cloud prediction algorithm. In particular, further work on either the clear sky LW or SW radiation code would be unlikely to improve the GCM performance.

7 Acknowledgement

Thanks are due to Martin Dix, who made the results of the CSIRO-9 AMIP runs available and interpolated them to the $2.5° \times 2.5°$ latitude and longitude grid using Harvey Davies' 'cif' processing procedures. Thanks are also due to Ian Watterson for vigorous discussions about the interpretation of the data, and to Martin Platt and Ross Mitchell for constructive comments during the review stage.

References

B. Barkstrom, E. Harrison, G. Smith, R. Green, J. Kibler, R. Cess, and The ERBE Science Team. Earth Radiation Budget Experiment ERBE archival and April 1985 results. *Bull. Amer. Meteorol. Soc.*, 70:1254–1262, 1989.

B.R. Barkstrom. The Earth Radiation Budget Experiment ERBE. *Bull. Amer. Meteorol. Soc.*, 65:1170–1185, 1984.

B.P. Briegleb, P. Minnis, V. Ramanathan, and E.F. Harrison. Comparison of clear-sky albedos inferred from satellite observations and model computations. *J. Clim. Appl. Meteorol.*, 25:214–226, 1986.

R.D. Cess, G.L. Potter, J.P. Blanchet, G.J. Boer, A.D. Del Genio, M. Déqué, V. Dymnikov, V. Galin, W.L. Gates, S.J. Ghan, J.T. Kiehl, A.A. Lacis, H. Le Treut, Z.-X. Li, X.-Z. Liang, B.J. McAvaney, V.P. Meleshko, J.F.B. Mitchell, J.-J. Morcrette, D.A. Randall, L. Rikus, E. Roeckner, J.F. Royer, U. Schlese, D.A. Sheinin, A. Slingo, A.P. Sokolov, K.E. Taylor, W.M. Washington, R.T. Wetherald, I. Yagai, and M.-H. Zhang. Intercomparison and interpretation of climate feedback processes in 19 atmospheric general circulation models. *J. Geophys. Res.*, 95D:16601–16615, 1990.

R.D. Cess, G.L. Potter, W.L. Gates, J-J. Morcrette, and L. Corsetti. Comparison of general circulation models to Earth Radiation Budget Experiment data: comparison of clear-sky fluxes. *J. Geophys. Res.*, 97D:20421–20426, 1992.

J.R. Garratt, P.B. Krummel, and E.A. Kowalczyk. The surface energy balance at local and regional scales—a comparison of general circulation model results with observations. *J. Clim.*, 6:1090–1109, 1993.

W.L. Gates. AMIP: The Atmospheric Model Intercomparison Project. *Bull. Amer. Meteorol. Soc.*, 73:1962–1970, 1992.

Harshvardhan, D.A. Randall, T.G. Corsetti, and D.A. Dazlich. Earth radiation budget and cloudiness simulations with a general circulation model. *J. Atmos. Sci.*, 46:1922–1942, 1989.

S.A. Klein and D.L. Hartmann. Spurious changes in the ISCCP data set. *Geophys. Res. Lett.*, 20:455–458, 1993.

L.P. Kopia. Earth Radiation Budget Experiment scanner instrument. *Rev. Geophys.*, 1986:400–406, 24.

A.A. Lacis and J.E. Hansen. A parameterization for the absorption of solar radiation in the earth's atmosphere. *J. Atmos. Sci.*, 31:118–133, 1974.

J.L. McGregor, H.B. Gordon, I.G. Watterson, M.R. Dix, and L.D. Rotstayn. The CSIRO 9-level atmospheric general circulation model. Technical Report 26, CSIRO Division of Atmospheric Research, 1992.

J.W. Posey and P.F. Clapp. Global distribution of normal surface albedo. *Geofisica Internacional*, 4:33–49, 1964.

A. Raval and V. Ramanathan. Observational determination of the greenhouse effect. *Nature*, 342:758–761, 1989.

W.B. Rossow. Measuring cloud properties from space: a review. *J. Clim.*, 2:201–213, 1989.

W.B. Rossow and R.A. Schiffer. ISCCP cloud data products. *Bull. Amer. Meteorol. Soc.*, 72:2–20, 1991.

M.D. Schwarzkopf and S.B. Fels. The simplified exchange method revisited: an accurate, rapid method for computation of infrared cooling rates and fluxes. *J. Geophys. Res.*, 96D:9075–9096, 1991.

P.J. Sellers, Y. Mintz, Y.C. Sud, and A. Dalcher. A simple biosphere model (SiB) for use within general circulation models. *J. Atmos. Sci.*, 43:505–531, 1986.

I.G. Watterson, M.R. Dix, J.L. McGregor, and H.B. Gordon. Surface air temperature and surface heat fluxes in simulated present and doubled CO_2 climates. *CSIRO Division of Atmospheric Research preprint*, 1993.

R.T. Wetherald, V. Ramaswamy, and S. Manabe. A comparative study of the observations of high clouds and simulations by an atmospheric general circulation model. *Climate Dynamics*, 5:135–143, 1991.

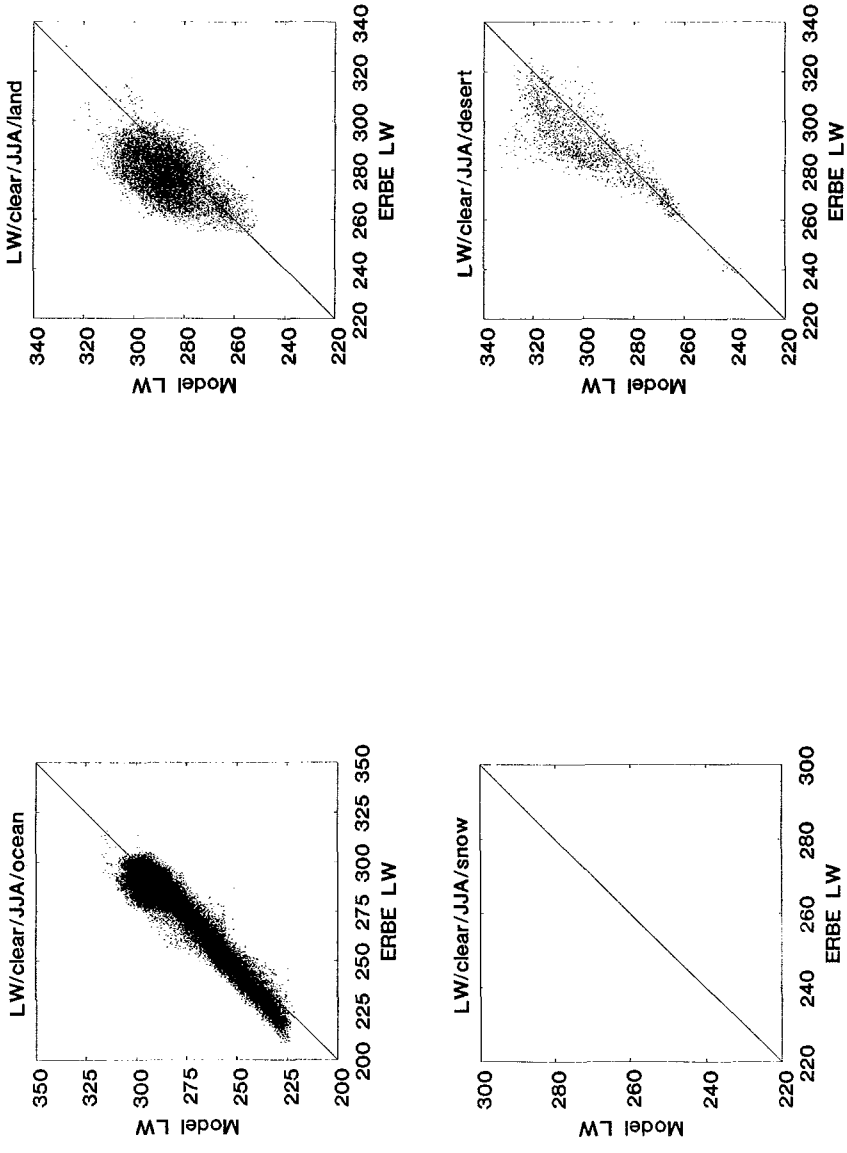

Figure 1: Comparison of the clear sky LW flux density predicted by the GCM and observed by ERBE for the JJA season. The units are Wm^{-2}. The ERBE surface classifications of ocean, land, snow and desert are shown separately.

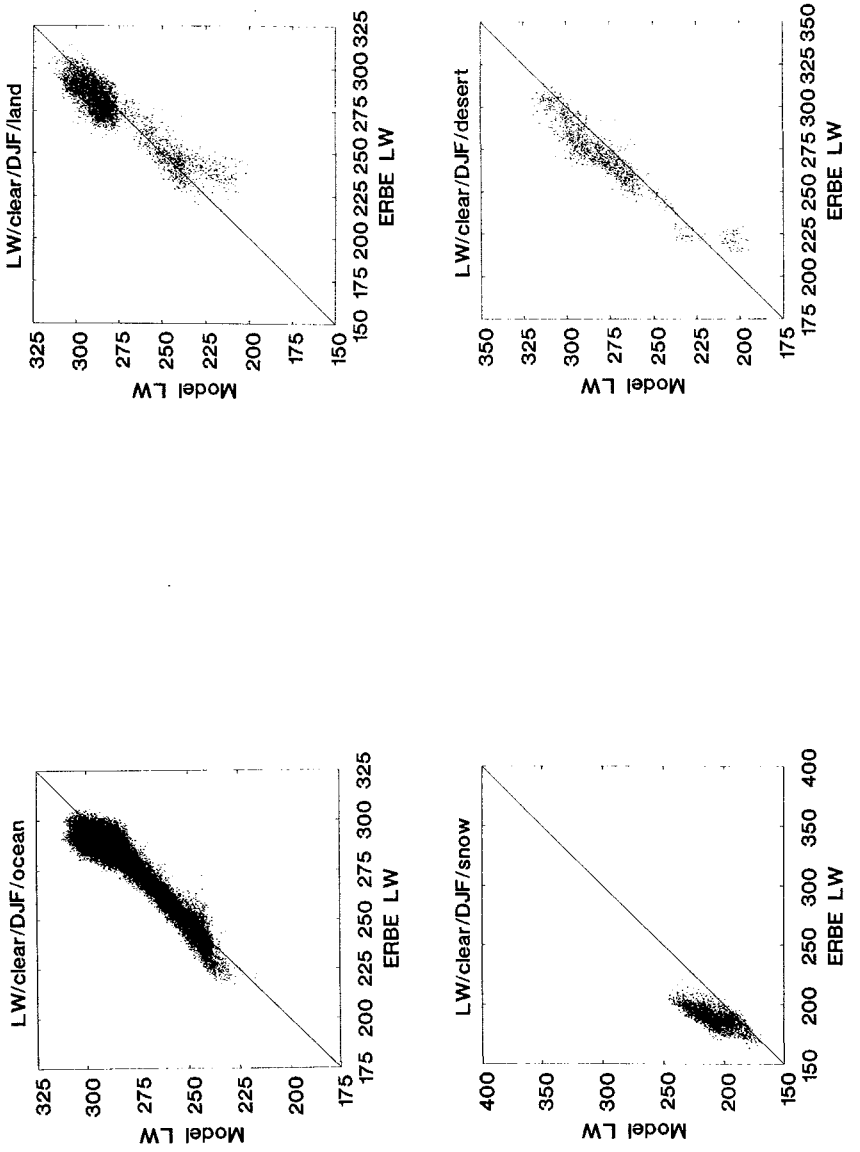

Figure 2: Comparison of the clear sky LW flux density predicted by the GCM and observed by ERBE for the DJF season. The units are Wm^{-2}. The ERBE surface classifications of ocean, land, snow and desert are shown separately.

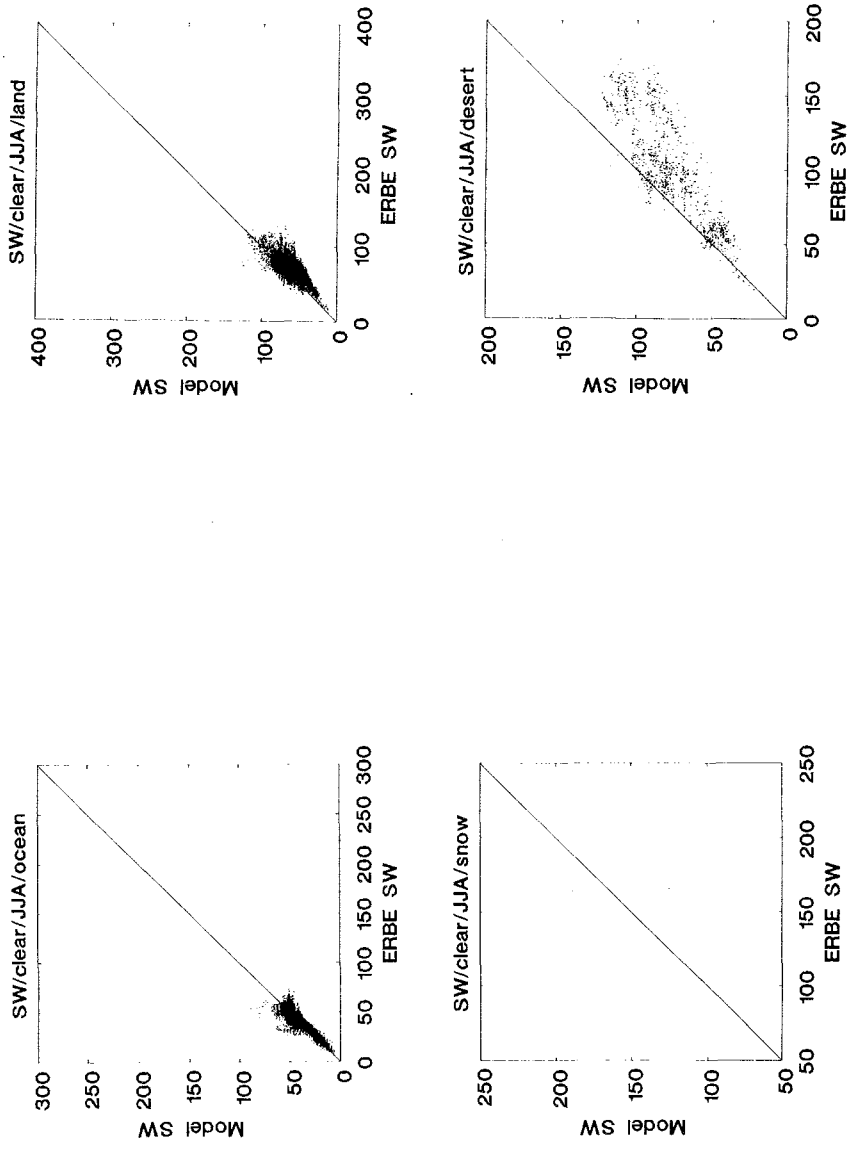

Figure 3: Comparison of the clear SW flux density predicted by the GCM and observed by ERBE for the JJA season. The units are Wm^{-2}. The ERBE surface classifications of ocean, land, snow and desert are shown separately.

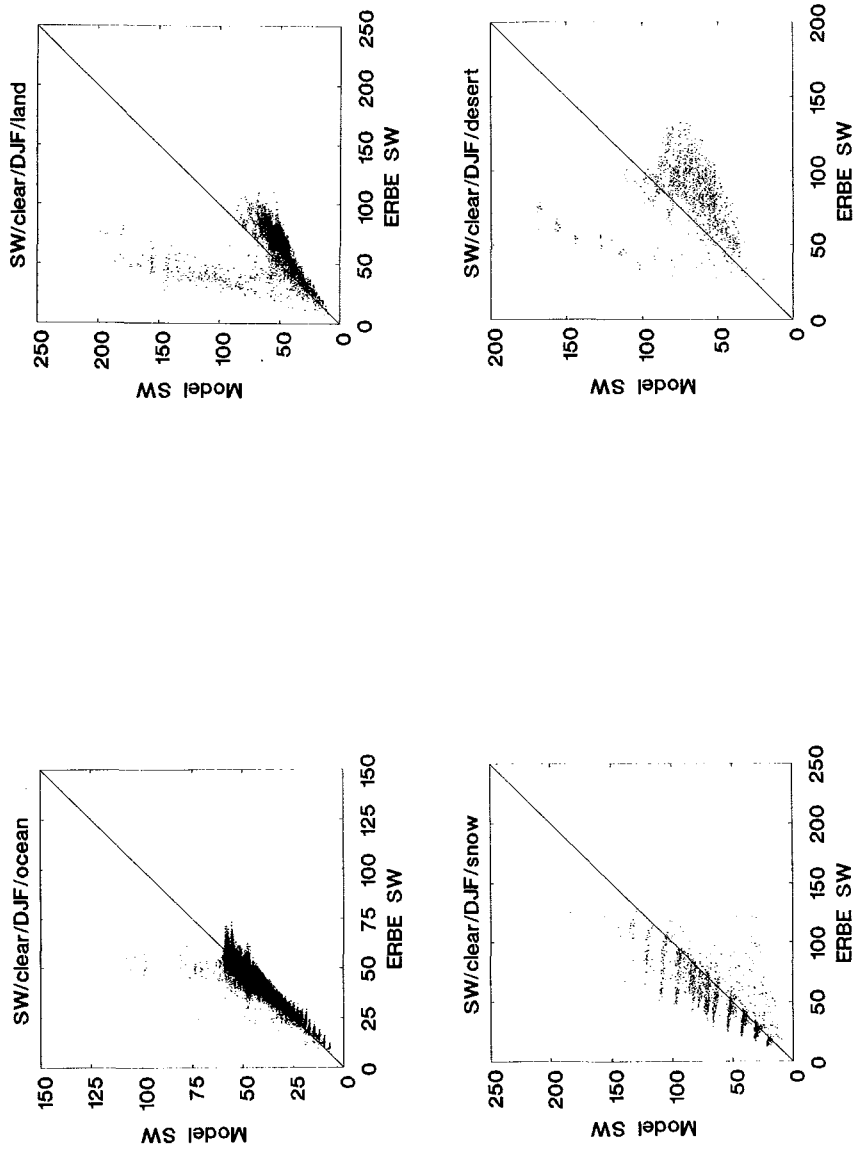

Figure 4: Comparison of the clear sky SW flux density predicted by the GCM and observed by ERBE for the DJF season. The units are Wm^{-2}. The ERBE surface classifications of ocean, land, snow and desert are shown separately.

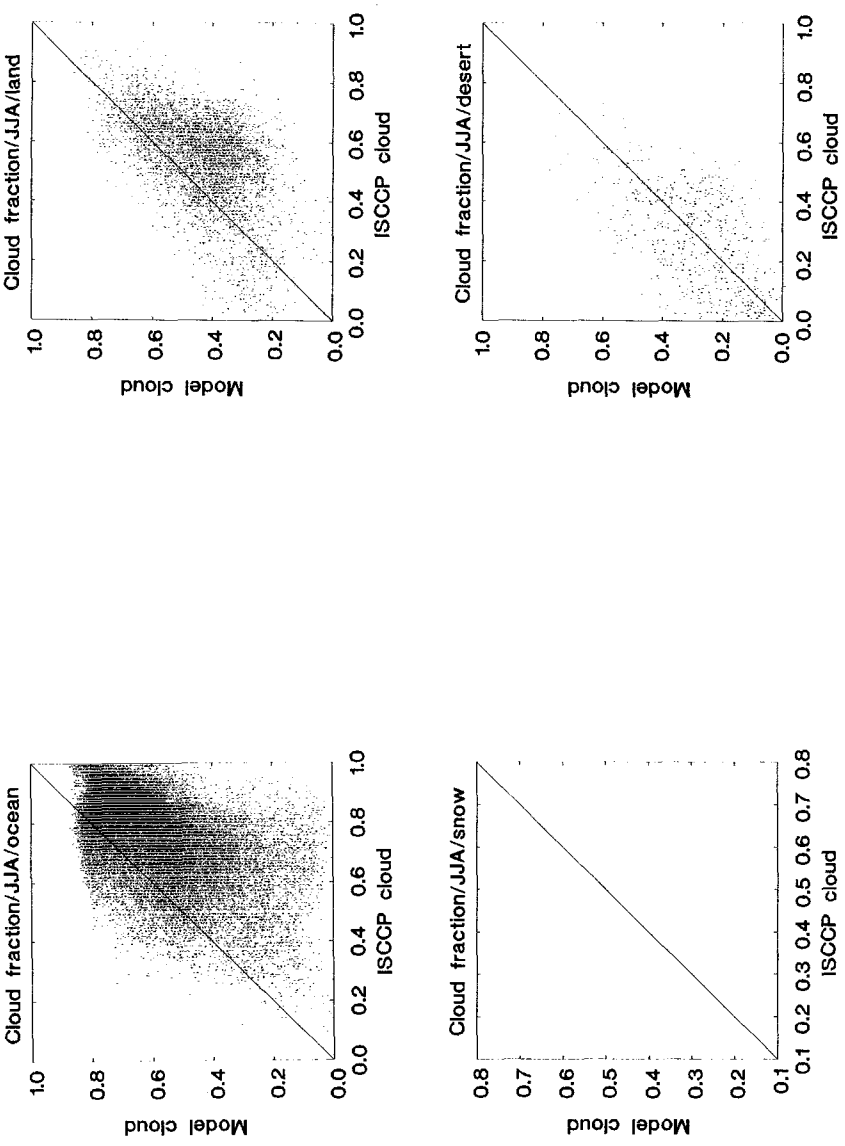

Figure 5: Comparison of cloud fraction predicted by the GCM and observed by ISCCP for the JJA season. The ERBE surface classifications of ocean, land, snow and desert are shown separately.

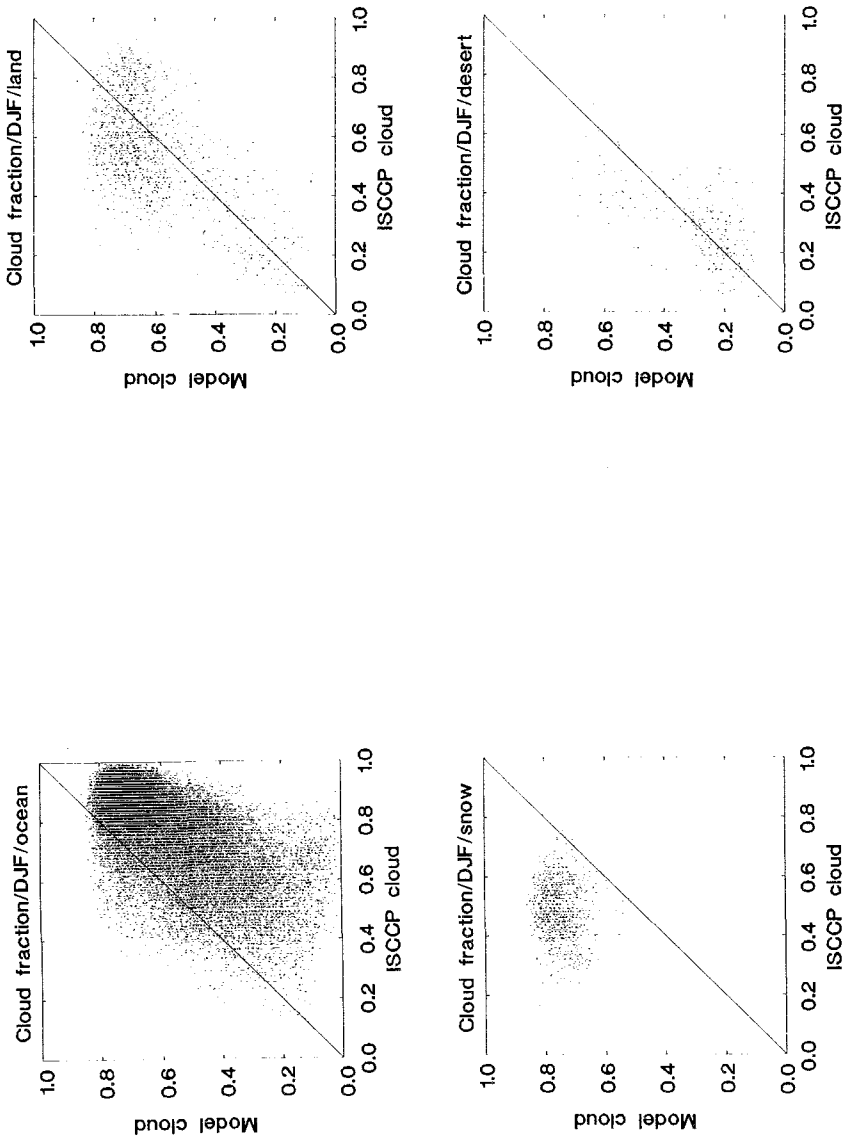

Figure 6: Comparison of cloud fraction predicted by the GCM and observed by ISCCP for the DJF season. The ERBE surface classifications of ocean, land, snow and desert are shown separately.

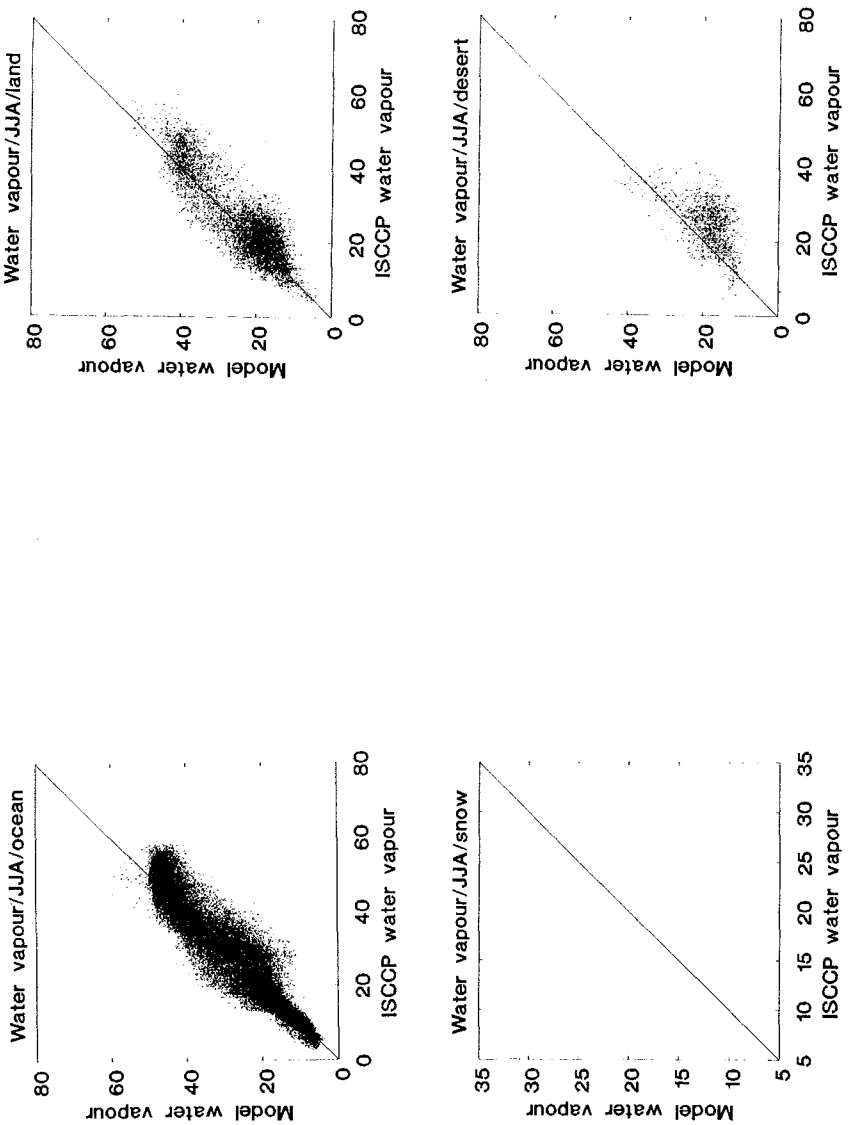

Figure 7: Comparison of water vapour column predicted by the GCM and retrieved from TOVS for the JJA season. The units are $kg\,m^{-2}$. The ERBE surface classifications of ocean, land, snow and desert are shown separately.

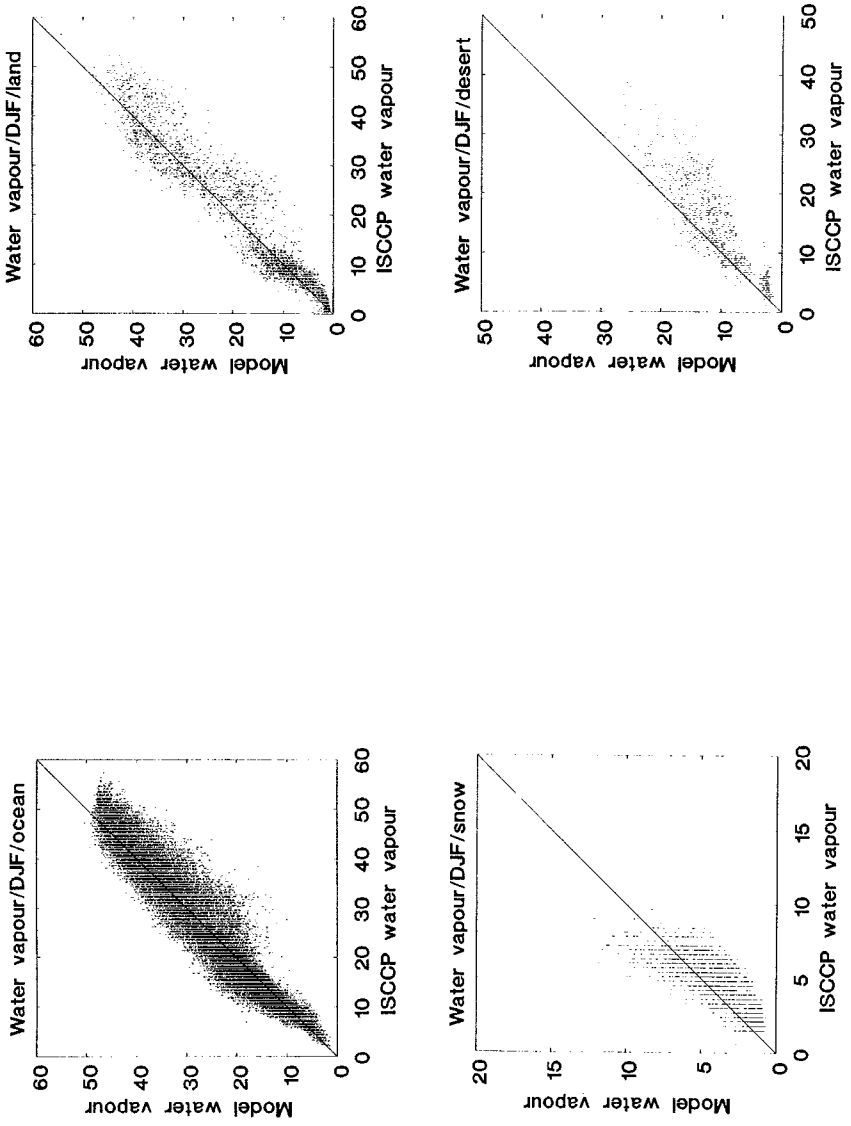

Figure 8: Comparison of water vapour column predicted by the GCM and retrieved from TOVS for the DJF season. The units are kg m^{-2}. The ERBE surface classifications of ocean, land, snow and desert are shown separately.

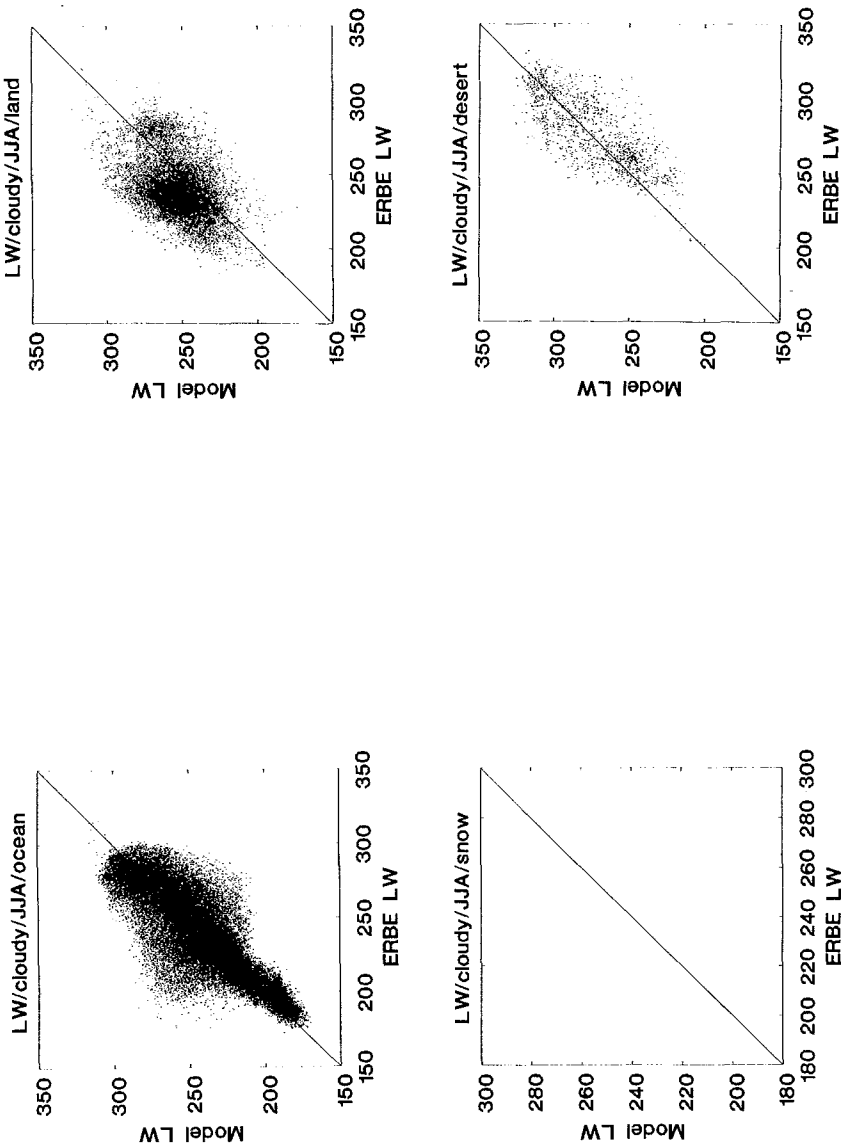

Figure 9: Comparison of the cloudy sky LW flux density predicted by the GCM and observed by ERBE for the JJA season. The units are Wm^{-2}. The ERBE surface classifications of ocean, land, snow and desert are shown separately.

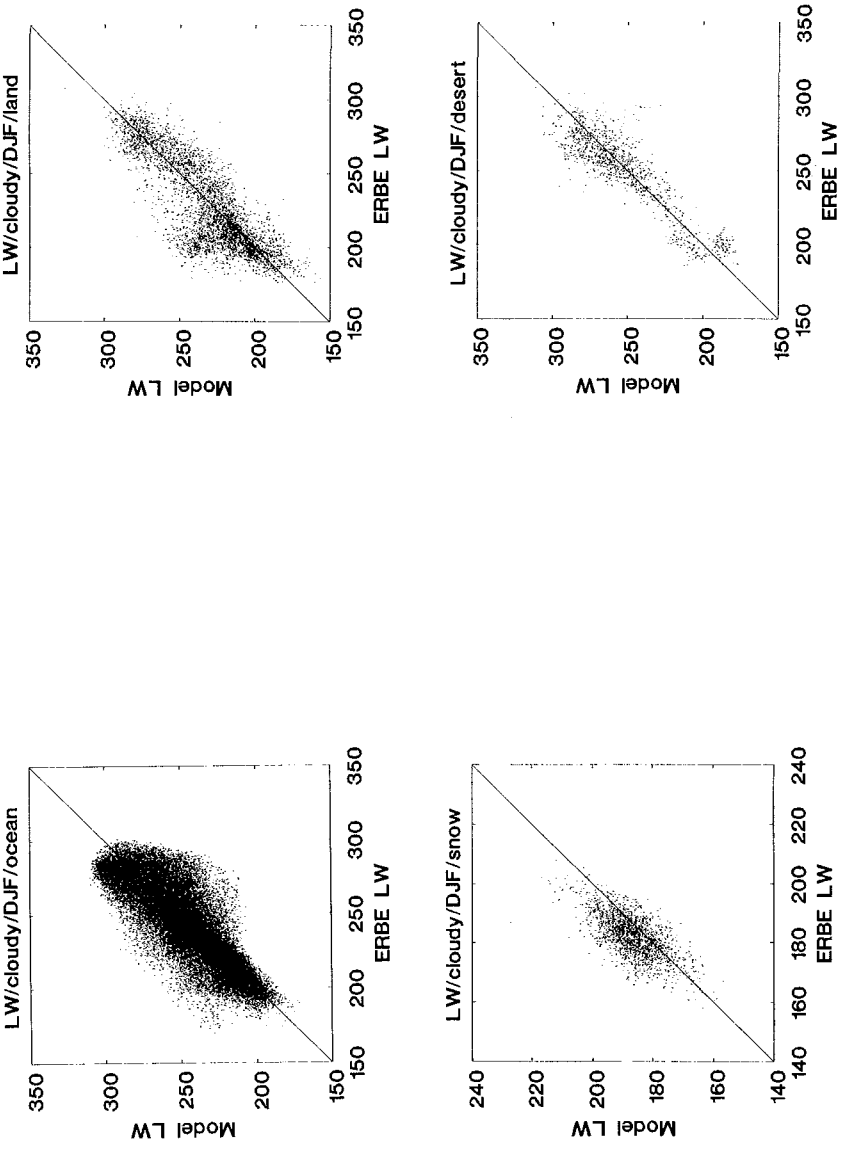

Figure 10: Comparison of the cloudy sky LW flux density predicted by the GCM and observed by ERBE for the DJF season. The units are Wm^{-2}. The ERBE surface classifications of ocean, land, snow and desert are shown separately.

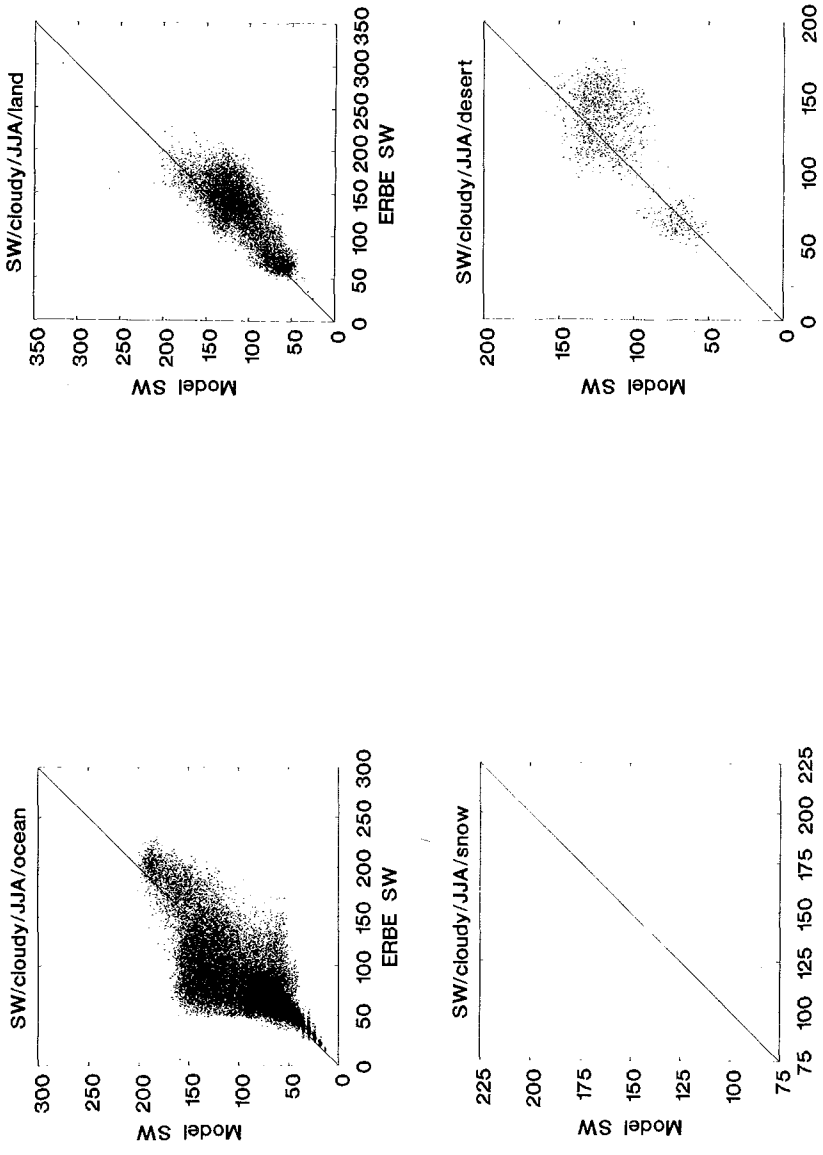

Figure 11: Comparison of the cloudy sky SW flux density predicted by the GCM and observed by ERBE for the JJA season. The units are Wm^{-2}. The ERBE surface classifications of ocean, land, snow and desert are shown separately.

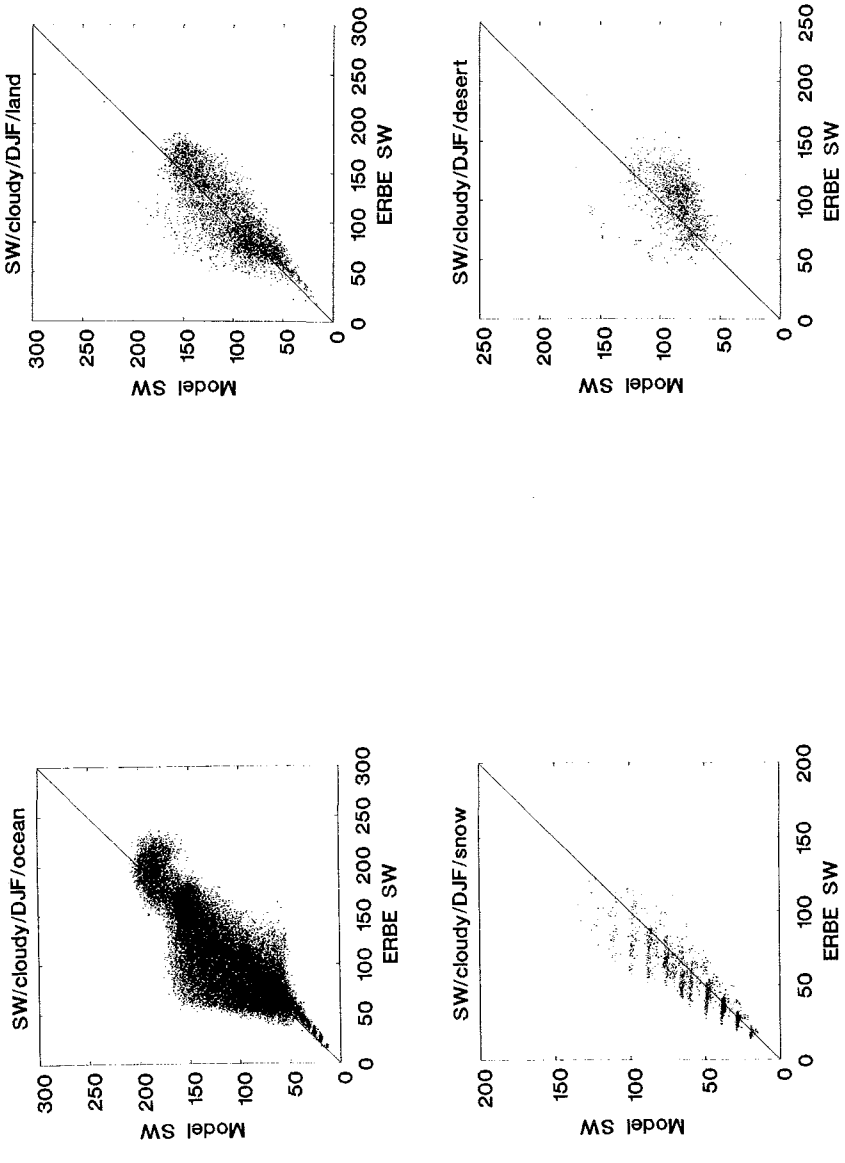

Figure 12: Comparison of the cloudy sky SW flux density predicted by the GCM and observed by ERBE for the DJF season. The units are Wm^{-2}. The ERBE surface classifications of ocean, land, snow and desert are shown separately.

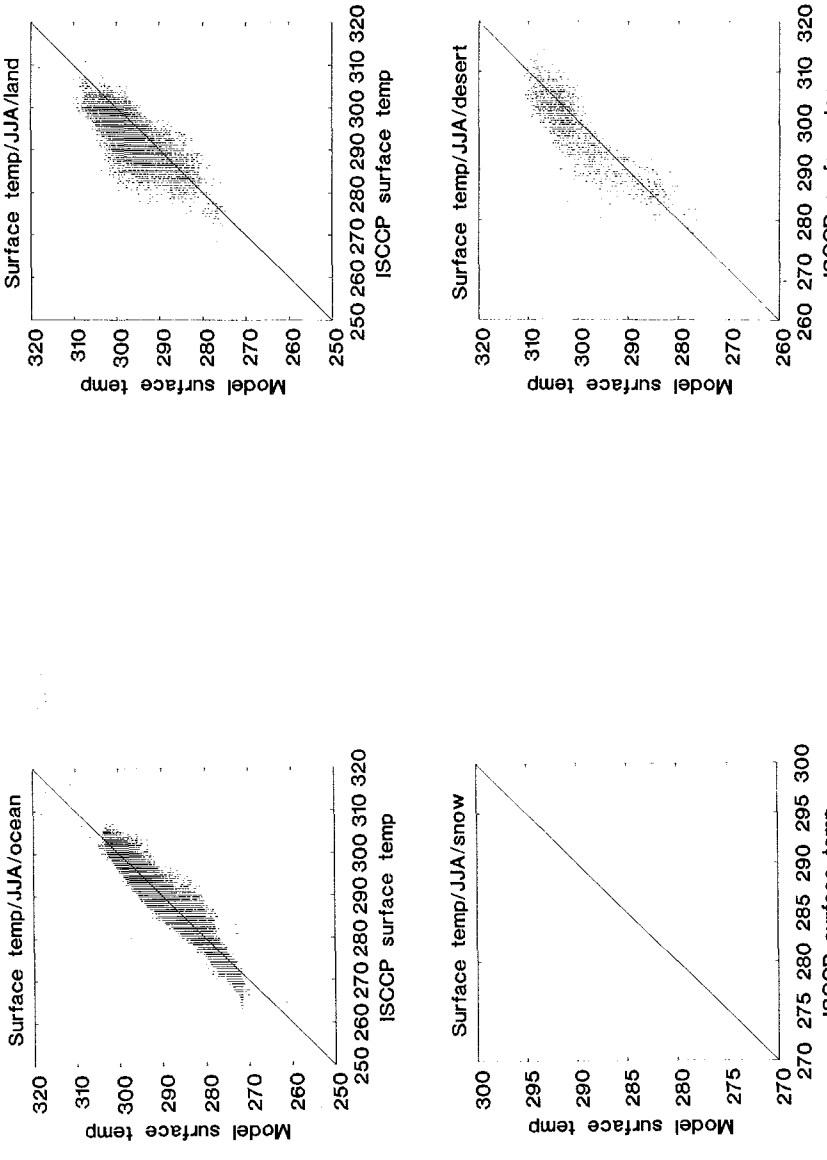

Figure 13: Comparison of the near surface temperature predicted by the GCM and retrieved from TOVS for the JJA season. Units are K. The ERBE surface classifications of ocean, land, snow and desert are shown separately.

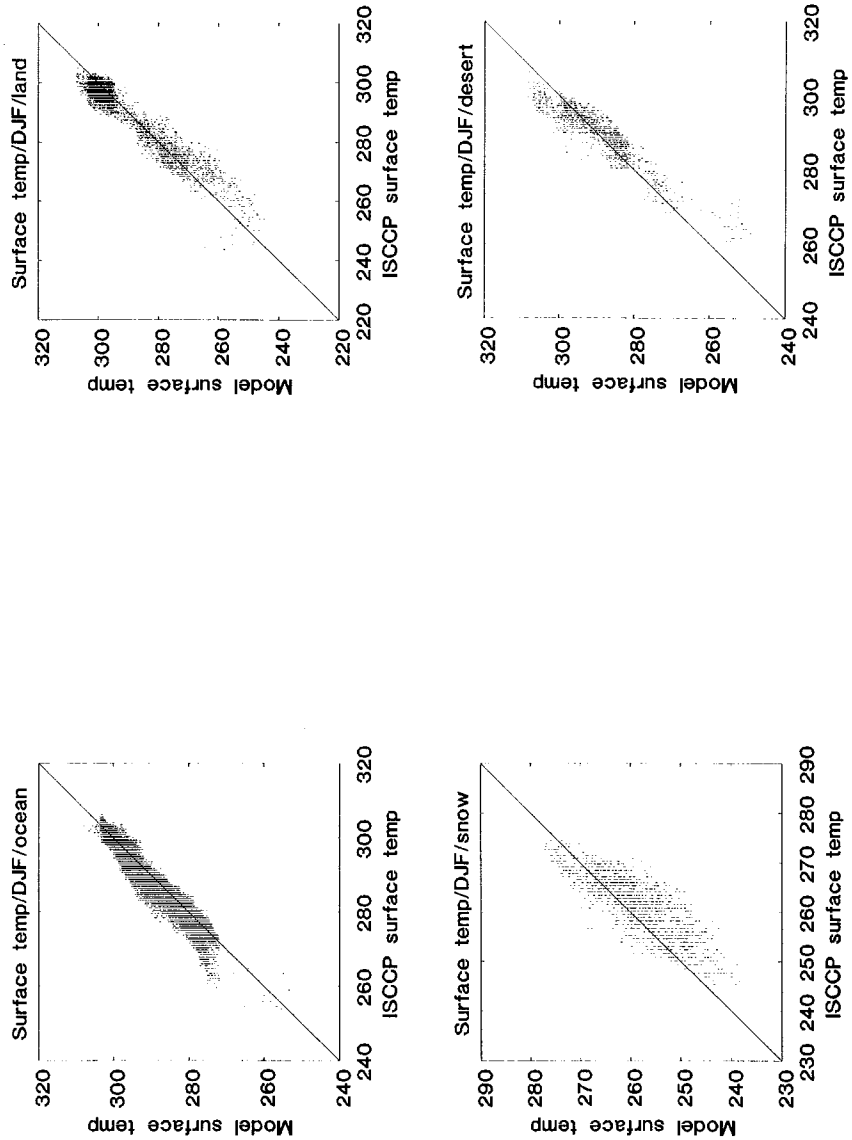

Figure 14: Comparison of the near surface temperature predicted by the GCM and retrieved from TOVS for the DJF season. Units are K. The ERBE surface classifications of ocean, land, snow and desert are shown separately.

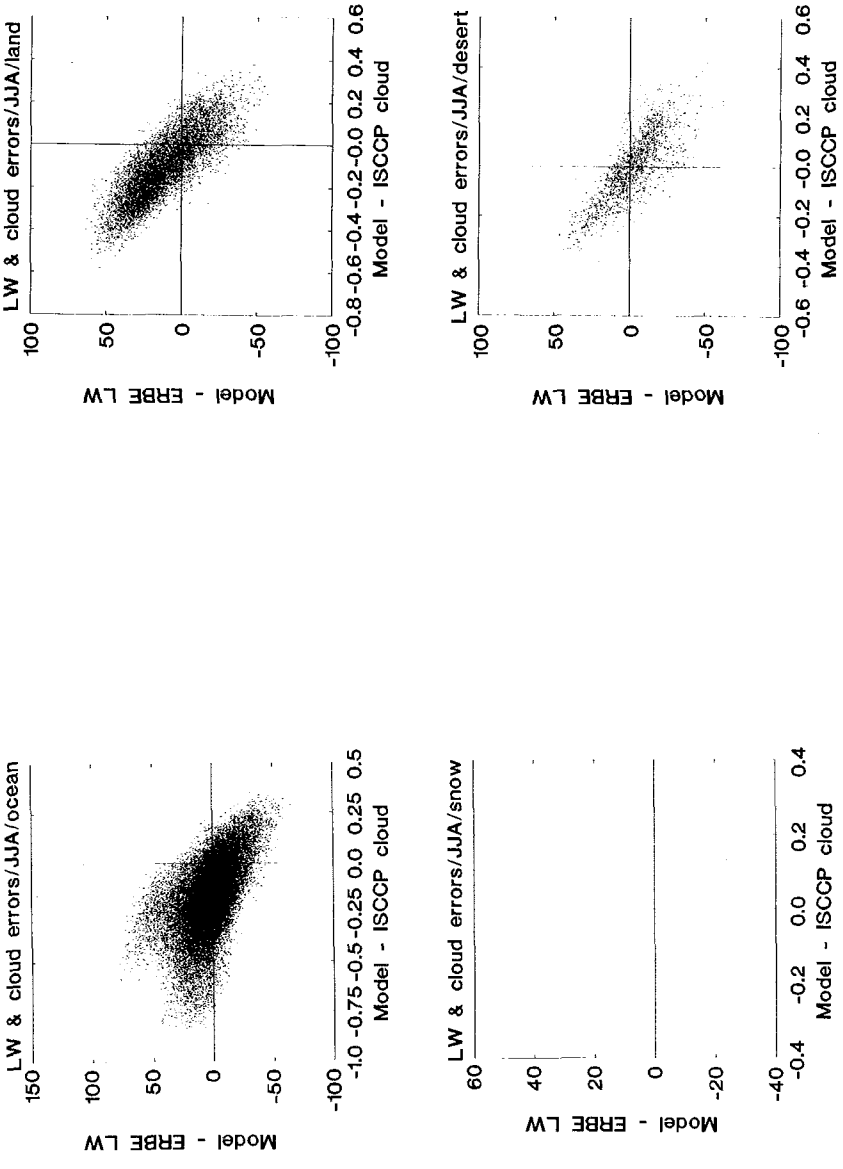

Figure 15: Correlation for the JJA season of ΔF_{LW}, the difference between the cloudy sky LW flux density predicted by the GCM and observed by ERBE, with ΔC, the difference between the cloud fraction predicted by the GCM and observed by ISCCP. The units of ΔF_{LW} are Wm^{-2}. The ERBE surface classifications of ocean, land, snow and desert are shown separately.

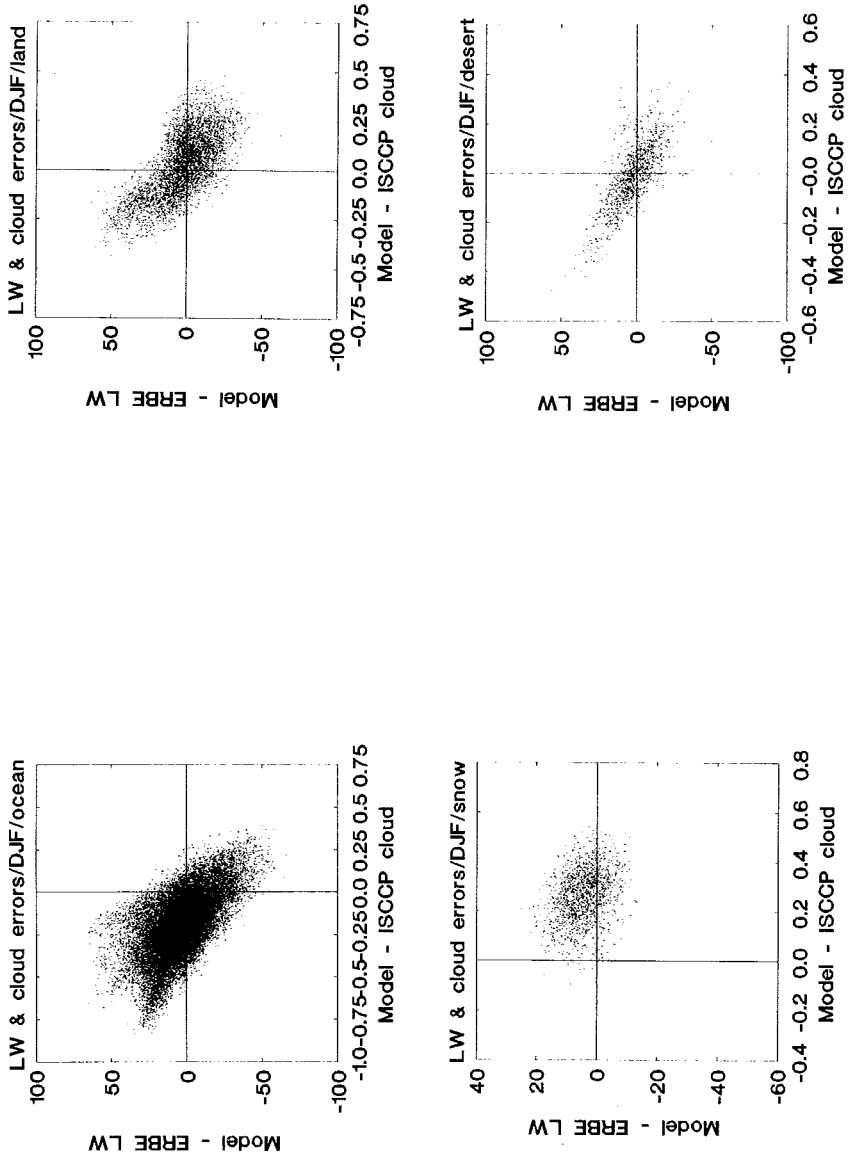

Figure 16: Correlation for the DJF season of ΔF_{LW}, the difference between the cloudy sky LW flux density predicted by the GCM and observed by ERBE, with ΔC, the difference between the cloud fraction predicted by the GCM and observed by ISCCP. The units of ΔF_{LW} are Wm^{-2}. The ERBE surface classifications of ocean, land, snow and desert are shown separately.

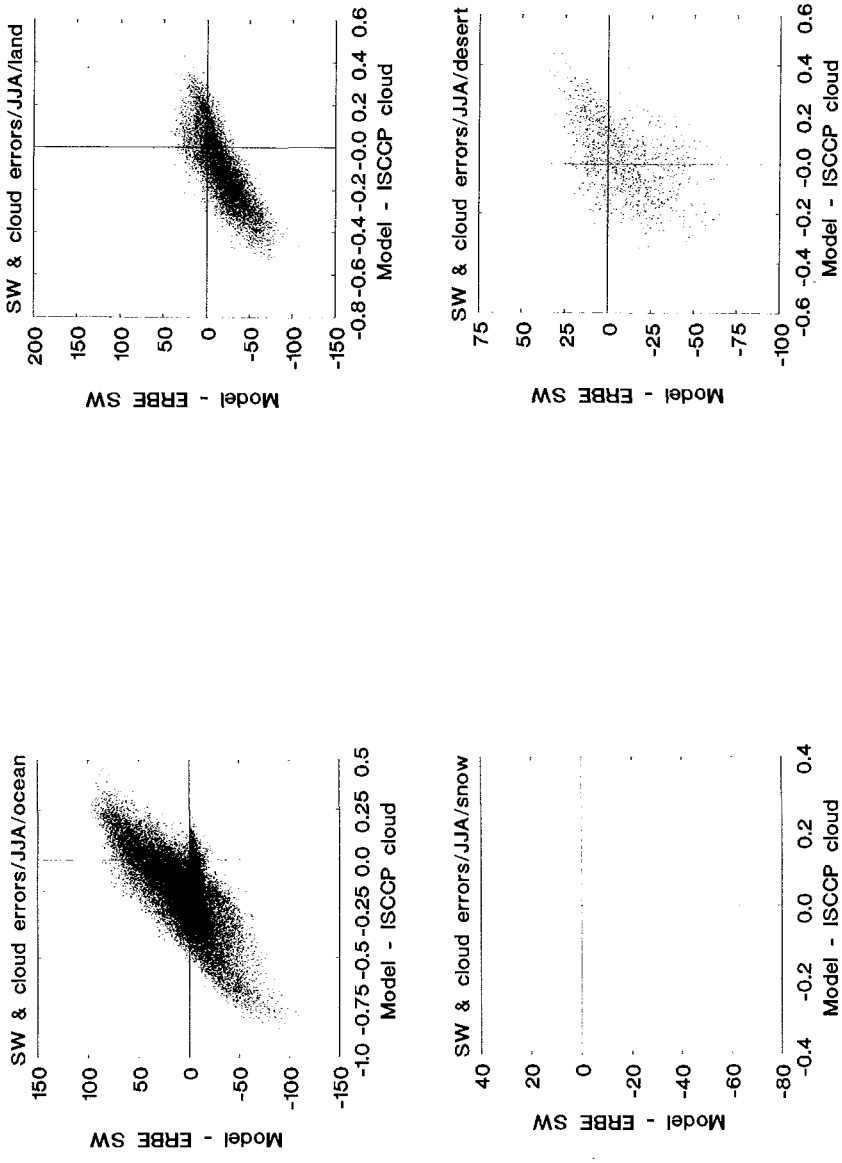

Figure 17: Correlation for the JJA season of ΔF_{SW}, the difference between the cloudy sky SW flux density predicted by the GCM and observed by ERBE, with ΔC, the difference between the cloud fraction predicted by the GCM and observed by ISCCP. The units of ΔF_{SW} are Wm^{-2}. The ERBE surface classifications of ocean, land, snow and desert are shown separately.

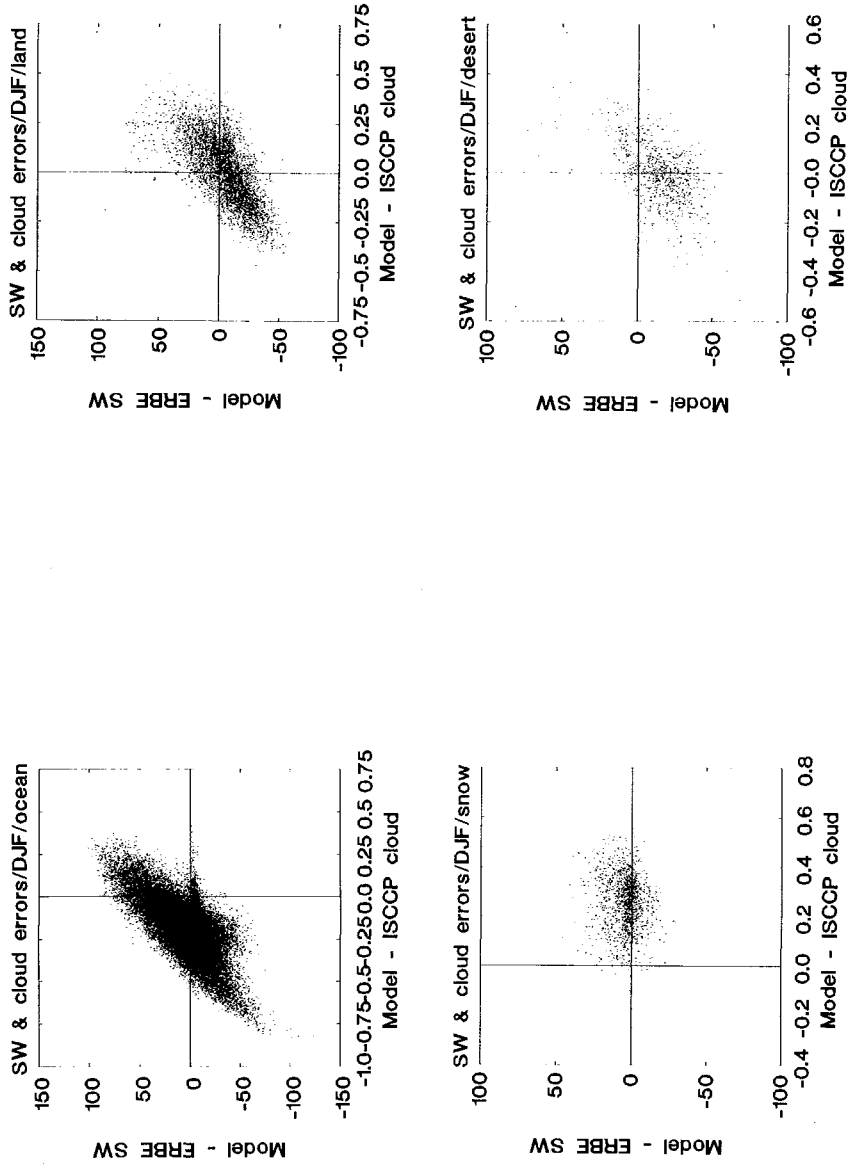

Figure 18: Correlation for the DJF season of ΔF_{SW}, the difference between the cloudy sky SW flux density predicted by the GCM and observed by ERBE, with ΔC, the difference between the cloud fraction predicted by the GCM and observed by ISCCP. The units of ΔF_{SW} are Wm^{-2}. The ERBE surface classifications of ocean, land, snow and desert are shown separately.

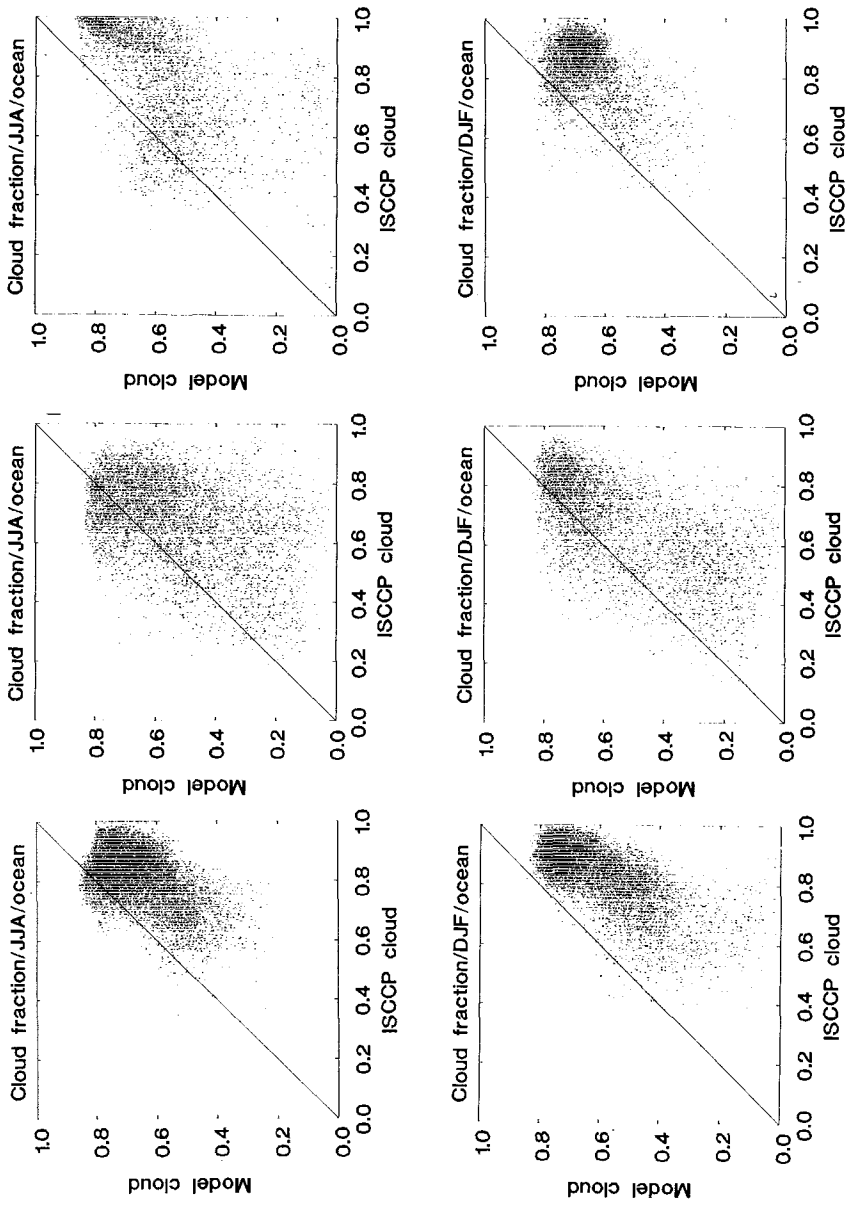

Figure 19: Comparison of the cloud fraction over the ocean predicted by the GCM and observed by ISCCP. The top row refers to the JJA season, while the bottom row is for DJF. The columns from left to right refer to the southern, tropical and northern zones (S, N and T) defined in the text.

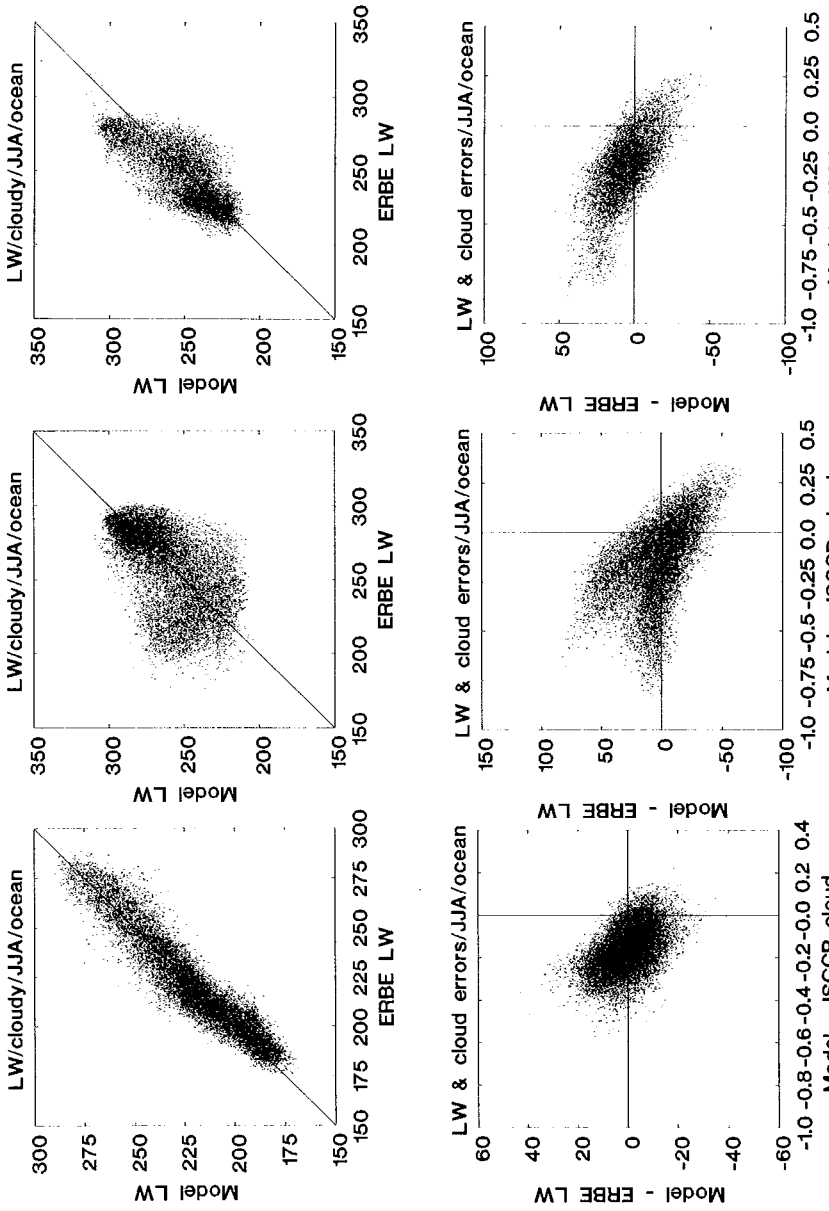

Figure 20: Regional analysis of the LW flux density, predicted by the GCM and measured by ERBE, for the JJA season over the ocean. The top row compares F_{LW}, while the second row correlates ΔF_{LW} with ΔC. The columns from left to right refer to the southern, tropical and northern zones (S, T and N) defined in the text.

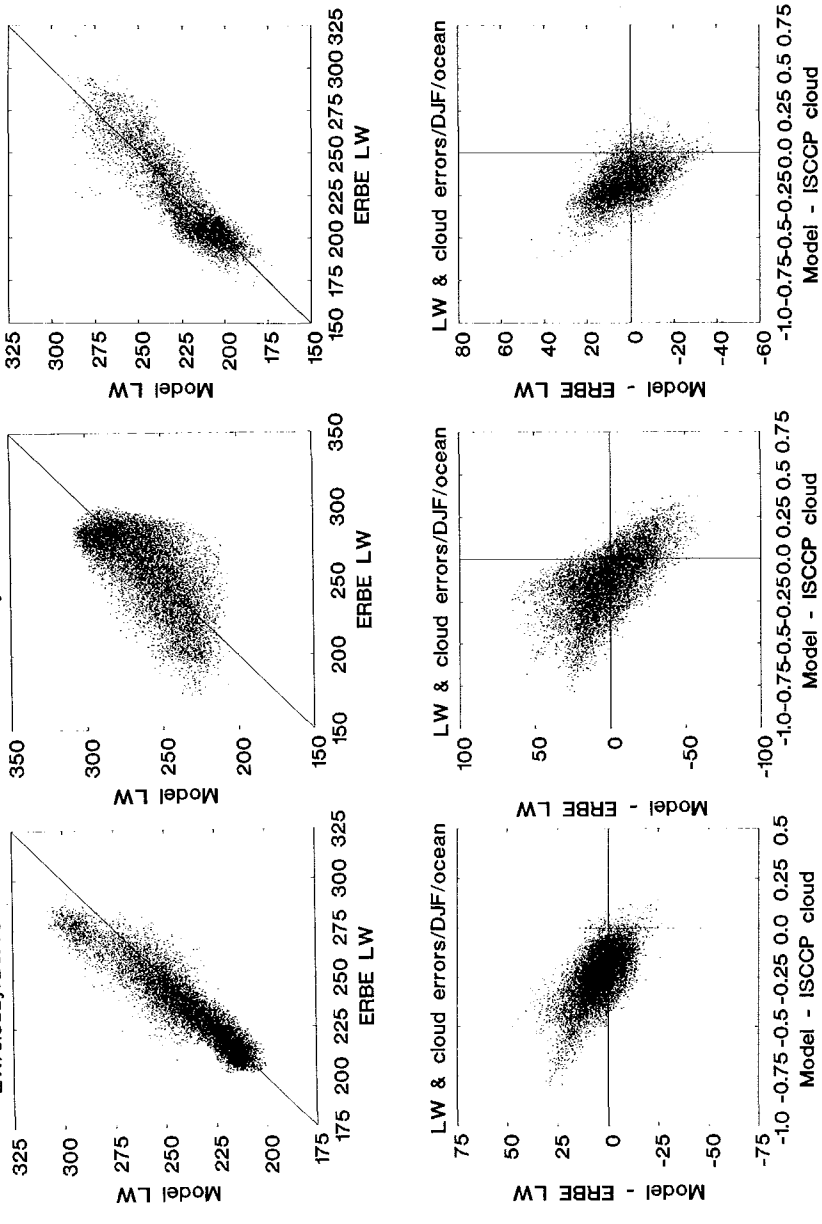

Figure 21: Regional analysis of the LW flux density, predicted by the GCM and measured by ERBE, for the DJF season over the ocean. The top row compares F_{LW}, while the second row correlates ΔF_{LW} with ΔC. The columns from left to right refer to the southern, tropical and northern zones (S, T and N) defined in the text.

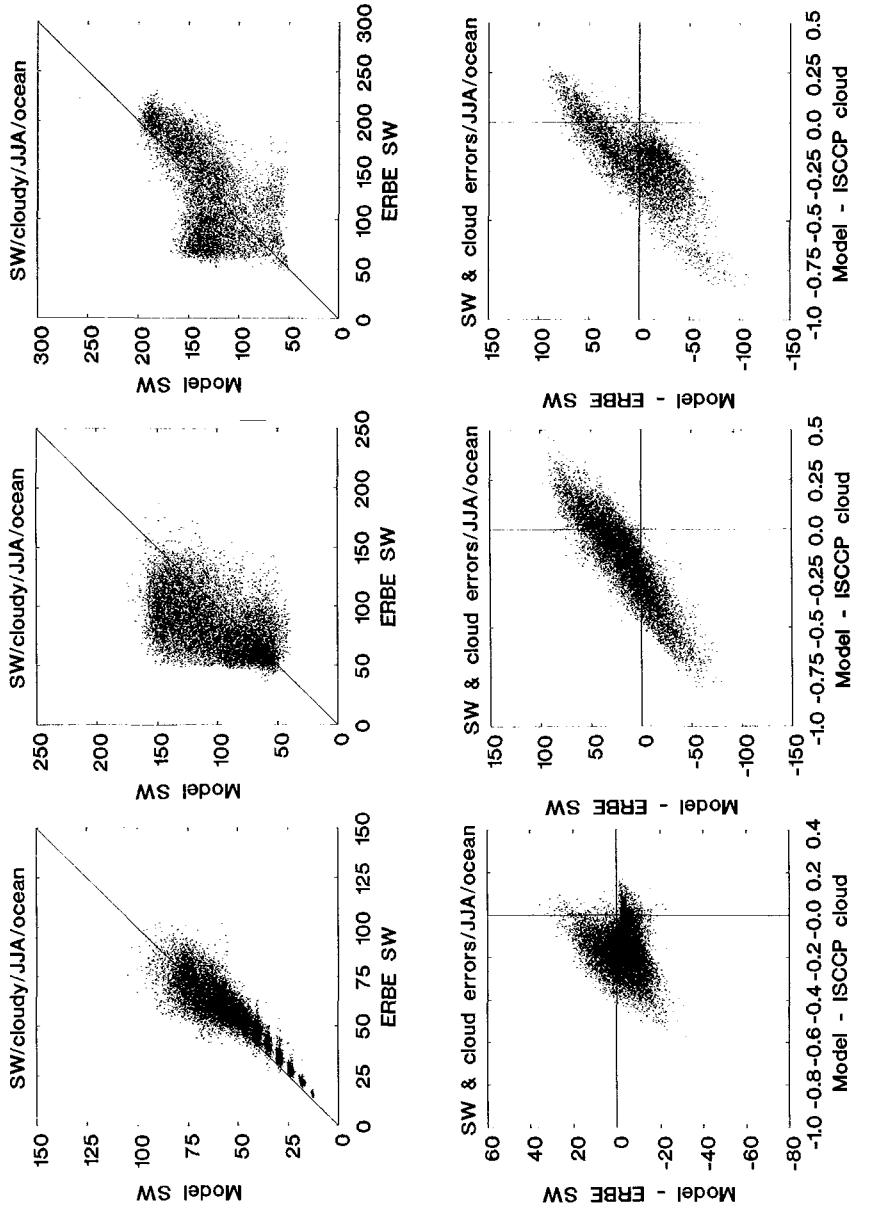

Figure 22: Regional analysis of the SW flux density, predicted by the GCM and measured by ERBE, for the JJA season over the ocean. The top row compares F_{SW}, while the second row correlates ΔF_{SW} with ΔC. The columns from left to right refer to the southern, tropical and northern zones (S, T and N) defined in the text.

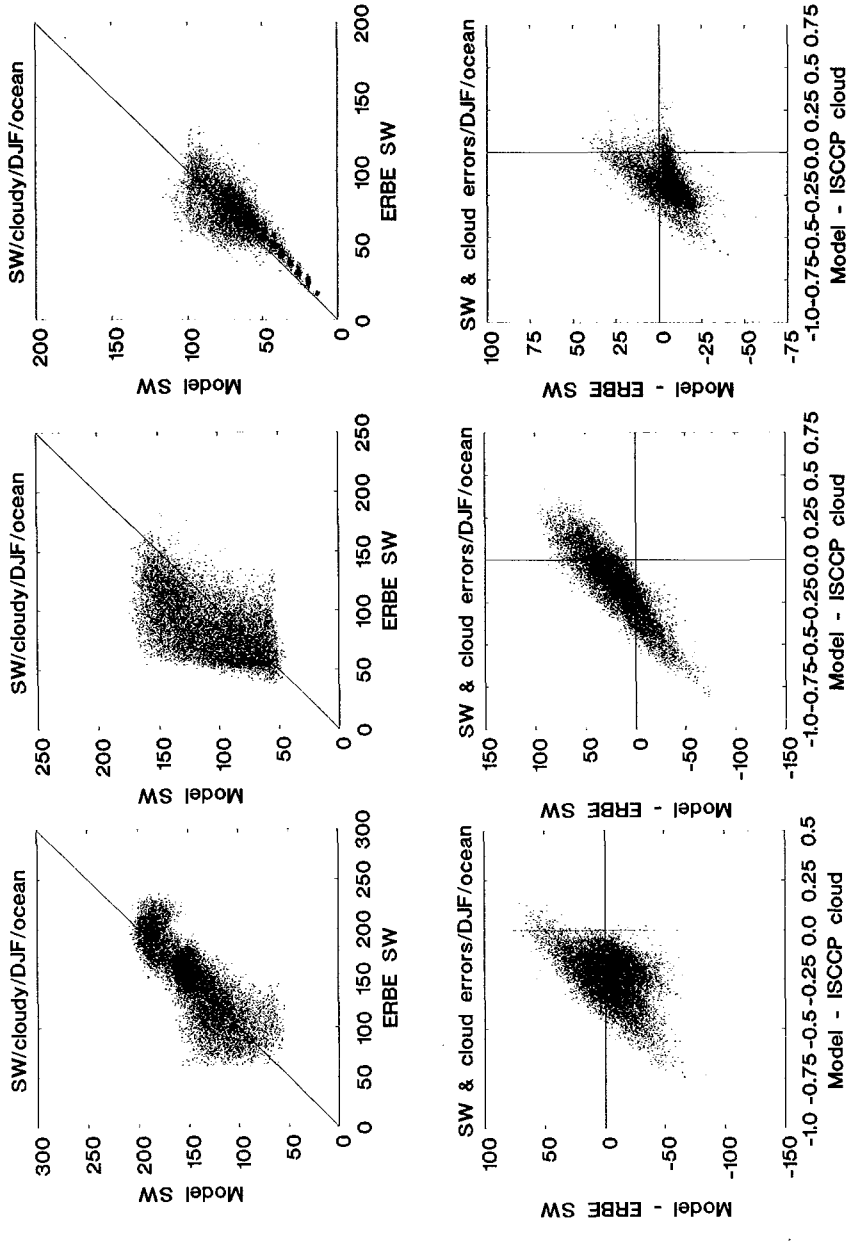

Figure 23: Regional analysis of the SW flux density, predicted by the GCM and measured by ERBE, for the DJF season over the ocean. The top row compares F_{SW}, while the second row correlates ΔF_{SW} with ΔC. The columns from left to right refer to the southern, tropical and northern zones (S, T and N) defined in the text.